THE UNIVERSITY OF CHICAGO

# SEARCH FOR THE RARE DECAY $K_L^0 \to \pi^0 \nu\bar{\nu}$

A DISSERTATION SUBMITTED TO
THE FACULTY OF THE DIVISION OF THE PHYSICAL SCIENCES
IN CANDIDACY FOR THE DEGREE OF
DOCTOR OF PHILOSOPHY

DEPARTMENT OF PHYSICS

BY
JIASEN MA

CHICAGO, ILLINOIS
AUGUST 2009

# ABSTRACT

A search for $K_L^0 \to \pi^0\nu\bar{\nu}$ was performed on data taken during the last Run of the E391a experiment at KEK. Blind analysis approach was adopted. The acceptance for the signal was improved from previous analysis by about 40% because of a better understanding of the background. With $(3.48 \pm 0.25) * 10^9$ $K_L^0$ decays, we found no candidate events. An upper limit of $6.96 \times 10^{-8}$ on the $K_L^0 \to \pi^0\nu\bar{\nu}$ branching ratio was set at the 90% confidence level.

# ACKNOWLEDGMENTS

When I started six years ago at the University of Chicago, I didn't choose high energy experiment. If I have the chance to do it again, I certainly will choose to work in high energy physics, and work on this challenging experiment - searching for $K_L^0 \to \pi^0\nu\bar{\nu}$. I am grateful to my advisor, Yau W. Wah for giving the wonderful experience that would change my mind in that scenario. Through his instruction and observing his own daily work, I learned the importance of focusing on the right problem. His wisdom, guidance and insights in high energy experiment were critical to my thesis work. I should also thank Wah for his support in whatever things I try.

I would like to thank Gabe Perdue and Jon Nix. I had consumed too much of their time by asking them just about everything on the E391a experiment while they were here.

I should thank Hideki Morii for his contributions in this work. From the RunIII data taking to now, we had worked closely to get the job done.

I want to thank Takao Inagaki for teaching me different aspects on the experiment.

I want to thank Joseph Comfort for introducing Fluka to me.

I would also like to thank all of my other collaborators in E391a, who has made this ambitious experiment possible. I benefited a lot from conversations with Taku Yamanaka, Tadashi Nomura, Hajime Nanjo, Kai-Feng Chen, Gei Youb Lim, Mitsuhiro Yamaga, Takeshi Komatsubara, Hiroaki Watanabe, Mikhail Doroshenko, Ken Sakashita, Toshi Sumida, and many others. They were also very warm to help me get around while I was in Japan.

I thank my parents, my aunt and my sister, who have worked hard, supported me, and opened the door of education to me. My special thank goes to my wife, who has put up with my long graduate student life and supported me all the time. For my daughter, I will have more time to play with her after this thesis is done.

# TABLE OF CONTENTS

# LIST OF FIGURES

# LIST OF TABLES

# CHAPTER 1

# INTRODUCTION

CPT symmetry is a center piece of the particle physics. It stands for the invariance of physics laws under the following three discrete transformations:

- C-charge conjugation, exchanging particles and anti-particles
- P-parity change, inverting the space
- T-time reversal, changing the time coordinate t into -t

There is a long history of study on the symmetry under the transformation of C, P, T and the combination of them [1][2][3][4]. The breaking of the symmetry under the Charge Conjugation and Parity transformation(CP violation), in particular, is still of great interest. The CP violation magnitude in the Standard Model is too small to explain the matter-dominant universe [5]. More information is needed on CP violation to test models beyond the Standard Model.

$K_L^0 \to \pi^0 \nu\bar{\nu}$ is a unique rare Kaon decay. Its branching ratio is proportional to the CP violation parameter in the Standard Model directly. This branching ratio is also calculated with little theoretical uncertainty in the Standard Model. Any deviation of a measurement from the theoretical prediction will be a clear signal for new physics. The search for this decay and the measurement of the branching ratio is of great interest for testing the Standard Model. In particular, it is a powerful probe to the origin of CP violation in the quark sector.

## 1.1 $K_L^0 \to \pi^0 \nu\bar{\nu}$ in the Standard Model

In this section we will describe how $K_L^0 \to \pi^0 \nu\bar{\nu}$ fits in the Standard Model. We will review 1) the Kaon phenomenology of CP violation, 2) CP violation and the CKM matrix

in the Standard Model, and 3) the Standard Model prediction for the branching ratio of $K_L^0 \to \pi^0 \nu\bar{\nu}$.

### *1.1.1 Kaon phenomenology of CP violation*

Neutral Kaons are produced by the strong interaction in the eigenstates of strangeness: $K^0$ and $\bar{K}^0$. They are formed by the combination of a strange quark and a down quark:

$$\begin{aligned} K^0 &= \begin{pmatrix} d \\ \bar{s} \end{pmatrix} \quad (S = +1)\,, \\ \bar{K^0} &= \begin{pmatrix} \bar{d} \\ s \end{pmatrix} \quad (S = -1)\,. \end{aligned} \tag{1.1}$$

Through mixing shown in Figure 1.1, the particles we observe in the laboratory are actually the linear combinations of them:

$$\begin{aligned} |K_1^0> &= \frac{1}{\sqrt{2}} \left( |K^0> + |\bar{K}^0> \right), \\ |K_2^0> &= \frac{1}{\sqrt{2}} \left( |K^0> - |\bar{K}^0> \right), \end{aligned} \tag{1.2}$$

where the $CP$ eigenvalue of $|K_1^0>$ is +1, and -1 for $|K_2^0>$.

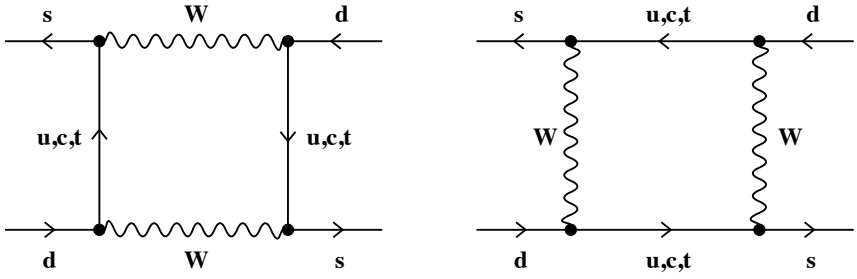


Figure 1.1: Diagrams mediating $K^0$ and $\bar{K}^0$ mixing.

One implication from this is that $K_1^0$ should decay into two pions as $K_2^0$ should decay into three pions to conserve the CP eigenvalues in the initial states. And the the two pion

decay or the $K_1^0$ decay should be faster since there is more energy released.

This beautiful and simple picture was found to be broken in 1964 [3] by the discovery of $K_L^0 \to \pi^+\pi^-$. To accommodate $K_L^0 \to \pi^+\pi^-$, an asymmetry is introduced in the mixing of $K^0$ and $\bar{K}^0$. So $K_L^0$ is not just $K_2^0$, but a superposition of $K_2^0$ and $K_1^0$:

$$\begin{aligned} K_L^0 &= \frac{K_2 + \epsilon K_1}{\sqrt{1+\epsilon^2}}, \\ K_S^0 &= \frac{K_1 + \epsilon K_2}{\sqrt{1+\epsilon^2}}, \end{aligned} \tag{1.3}$$

We call this the indirect CP violation.

The type of CP violation which our interested process $K_L^0 \to \pi^0\nu\bar{\nu}$ is falls into the direct CP violation. In the direct CP violation, one CP eigenstate decays into the other. The existence of direct CP violation was established just about 10 years ago [6][7]. It was found through the measurement of the ratio of the four different decay branching ratio:

$$\frac{\Gamma(K_L \to \pi^+\pi^-)/\Gamma(K_S \to \pi^+\pi^-)}{\Gamma(K_L \to \pi^0\pi^0)/\Gamma(K_S \to \pi^0\pi^0)} \approx 1 + 6Re(\epsilon'/\epsilon), \tag{1.4}$$

where $\epsilon'$ is the parameter describing the direct CP violation. The current world average is: $\mathrm{Re}(\epsilon'/\epsilon) = (20.7 \pm 1.48_{stat} \pm 2.39_{syst}) \times 10^{-4} = (20.7 \pm 2.8) \times 10^{-4}$ [6]. The fact that it's non-zero says that direct CP violation exists.

### *1.1.2 CP violation in the Standard Model*

$K_L^0 \to \pi^0\nu\bar{\nu}$ is a Flavor-Changing Neutral Current process induced by the charged-current at the loop level. The flavor-changing charged current is precisely where the quark-sector CP violation comes in the Standard Model. The Lagrangian of this interaction is:

$$\mathcal{L}_{CC} = \frac{g}{\sqrt{2}} \left[ \bar{u}_i V_{ij} d_j W^- + \bar{d}_j V_{ij}^* u_i W^+ \right], \tag{1.5}$$

Under a CP operation, this becomes:

$$\mathcal{L}_{CC} = \frac{g}{\sqrt{2}} \left[ \bar{d}_j V_{ij} u_i W^+ + \bar{u}_i V_{ij}^* d_j W^- \right], \tag{1.6}$$

$V_{ij}$ is the CKM matrix. It determines the quark coupling from different generations. If $V_{ij}$ is a complex number, CP is not conserved. We will discuss the CKM matrix as follows:

A general $3 \times 3$ unitary matrix, like the CKM matrix, has nine free real parameters. But this number is reduced to four by the definition of the quark phases. There are several popular parametrizations of the CKM matrix. One uses three Euler angles ($\theta_{12}$, $\theta_{23}$, and $\theta_{31}$) and a CP-violating phase ($\delta$):

$$V = \begin{pmatrix} c_{12}\, c_{13} & s_{12}\, c_{13} & s_{13}\, e^{i\delta} \\ -s_{12}\, c_{23} - c_{12}\, s_{23}\, s_{13}\, e^{i\delta} & c_{12}\, c_{23} - s_{12}\, s_{23}\, s_{13}\, e^{i\delta} & s_{23}\, c_{13} \\ s_{12}\, c_{23} - c_{12}\, s_{23}\, s_{13}\, e^{i\delta} & -c_{12}\, c_{23} - s_{12}\, s_{23}\, s_{13}\, e^{i\delta} & c_{23}\, c_{13} \end{pmatrix} \tag{1.7}$$

with $c_{ij}$ defined as $\cos(\theta_{ij})$ and $s_{ij}$ defined as $\sin(\theta_{ij})$. If $\theta_{ij} = 0$, there will be no coupling between quark generation $i$ and quark generation $j$. In fact $\theta_{13}$ and $\theta_{23}$ are small [8].

In the Wolfenstein parametrization [9], the matrix is written as an expansion of $\lambda = |V_{us}| \approx 0.22$:

$$V = \begin{pmatrix} 1 - \lambda^2/2 & \lambda & A\,\lambda^3\,(\rho - i\,\eta) \\ -\lambda & 1 - \lambda^2/2 & A\,\lambda^2 \\ A\,\lambda^3\,(1 - \rho - i\,\eta) & -A\,\lambda^2 & 1 \end{pmatrix} + \mathcal{O}(\lambda^4) \tag{1.8}$$

This parametrization approximates the matrix to the order of $\lambda^3$. One nice thing about this

parametrization is that we can tell from the parametrization that CP is conserved to the order of $\lambda^2$, and only violated in the order of $\lambda^3$. The other nice thing is that $K_L^0 \to \pi^0 \nu\bar{\nu}$ branching ratio can be directly expressed in terms of the parameters in the Wolfenstein parametrization.

Applying the unitary property of the CKM matrix to the first and third columns of the matrix, we get:

$$V_{ub}^* V_{ud} + V_{cb}^* V_{cd} + V_{tb}^* V_{td} = 0. \tag{1.9}$$

This equation stands for a triangle in the complex plane if we take each of the three products of the matrix elements as a vector on the plane. The triangle is called the Unitary Triangle.

The area of this triangle is proportional to a fundamental quantity called Jarlskog parameter [10]. We denote it as $J$.

$$J = \mathrm{Im}\left[V_{ij} V_{kl} V_{kj}^* V_{il}^*\right] \quad (i \neq l, j \neq k). \tag{1.10}$$

In the Wolfenstein parametrization, $J \approx \lambda^6 A^2 \eta$. The value of $J$ is invariant under different parametrizations.

Since $V_{cd} V_{cb}^* = -A\,\lambda^3 + \mathcal{O}\left(\lambda^7\right)$, to an excellent approximation we can normalize $V_{cd} V_{cb}^*$ to 1 by scaling with $A\,\lambda^3$. The other two matrix element products scale as:

$$\frac{1}{A\,\lambda^3} V_{ud} V_{ub}^* = \bar{\rho} + i\,\bar{\eta} \qquad \frac{1}{A\,\lambda^3} V_{td} V_{tb}^* = 1 - (\bar{\rho} + i\,\bar{\eta})\,. \tag{1.11}$$

The sum of these three complex vectors closes (as it should by construction) as illustrated in Figure 1.2.

The current world average of the parameters in the Unitarity Triangle is listed in Table 1.1. For more comprehensive review of the parameters of the Unitarity Triangle and the

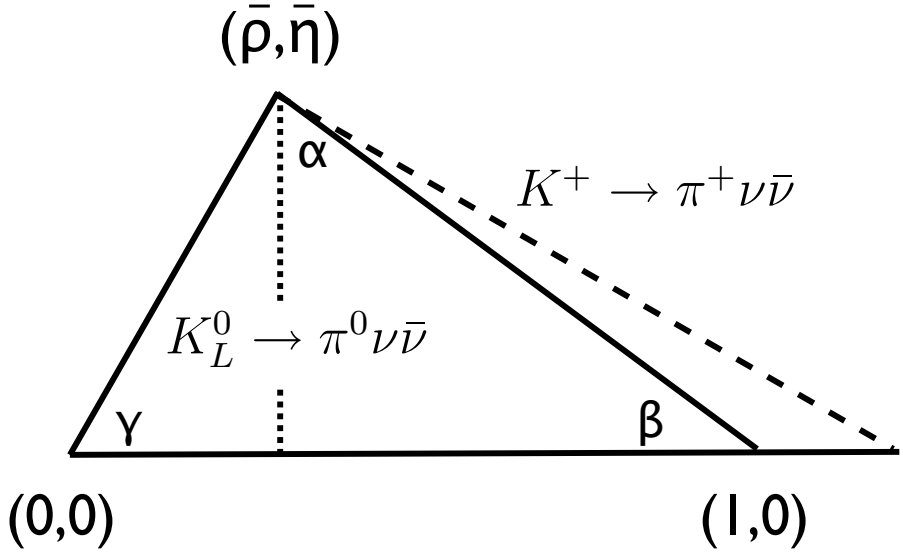


Figure 1.2: The Unitarity Triangle with the impacts of $K \to \pi\nu\bar{\nu}$ on the parameters visualized.

methods of their estimation, please refer to [11].

| Quantity | 1-$\sigma$ CL |
|---|---|
| $\lambda$ | $0.2265 + 0.0025 - 0.0023$ |
| $A$ | $0.801 + 0.029 - 0.020$ |
| $\bar{\rho}$ | $0.189 + 0.088 - 0.070$ |
| $\bar{\eta}$ | $0.358 + 0.046 - 0.042$ |

Table 1.1: Some key parameters of the Unitarity Triangle.

### *1.1.3 $K_L^0 \to \pi^0\nu\bar{\nu}$ Branching Ratio in the Standard Model*

$K_L^0 \to \pi^0\nu\bar{\nu}$ proceeds through penguin and box diagrams with internal quark exchanges as shown in Figure 1.3 [12]. By using the isospin relation, the matrix element in its decay branching ratio is extracted from the decay branching ratio of $K^+ \to \pi^0 e^+\nu$ with a very precise isospin breaking correction [13]. The theoretical uncertainty is less than 1%.

The branching ratio can be written as [12]:

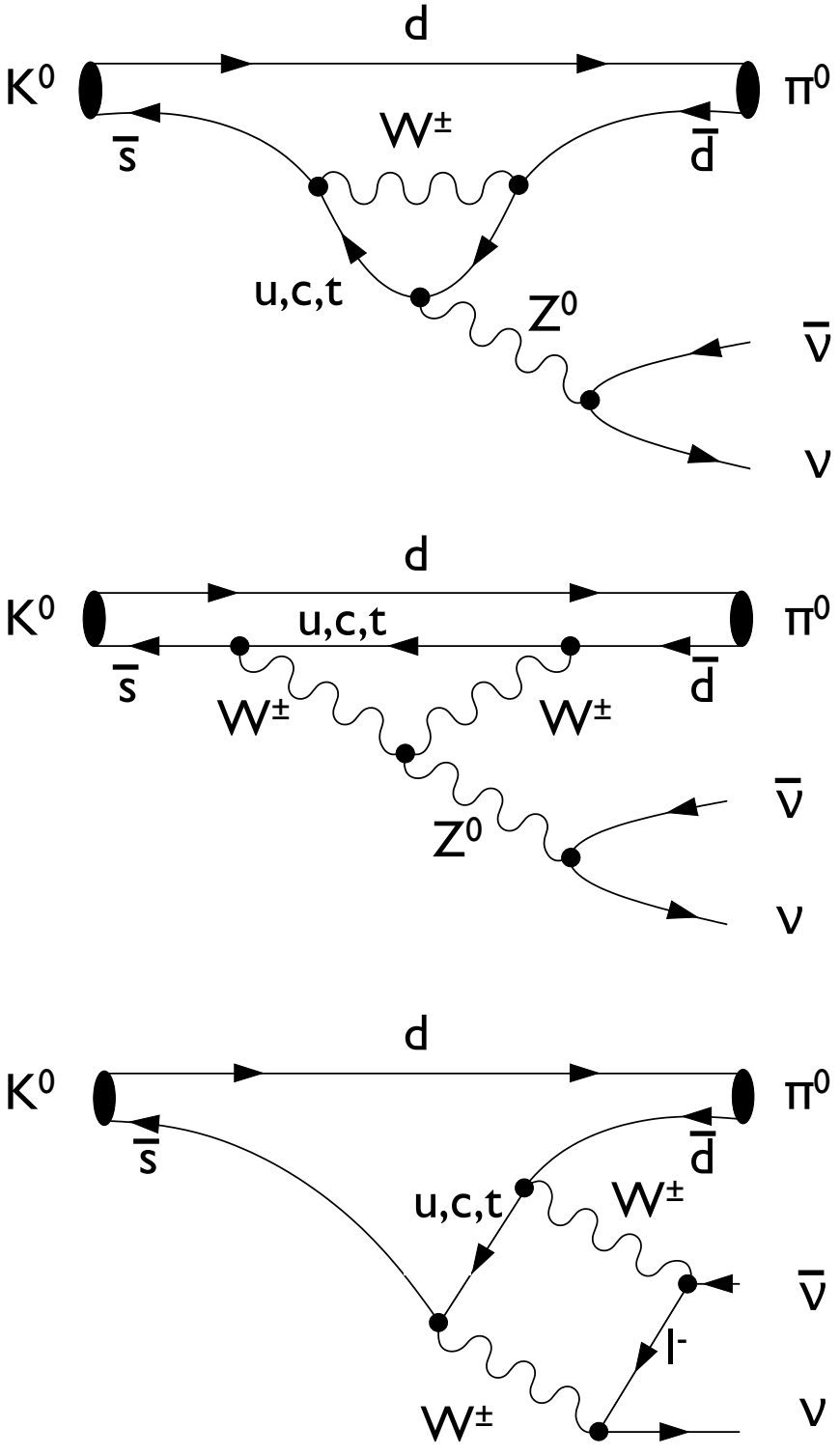


Figure 1.3: The penguin and box Feynman diagrams for $K_L^0 \to \pi^0 \nu\bar{\nu}$.

$$Br(K_L^0 \to \pi^0 \nu\bar{\nu}) = 6.87 \times 10^{-4} \times Br(K^+ \to \pi^0 e^+ \nu) \times A^4 \lambda^8 \eta^2 X^2(x_t) \tag{1.12}$$

where $x_t$ is the square of the top and W mass ratio, $x_t = m_t^2/m_w^2$, $X(x_t)$ is the Inami-Lim loop function [14] with QCD higher order correction.

As it is dominated by direct CP violation [12], $K_L^0 \to \pi^0 \nu\bar{\nu}$ branching ratio is directly proportional to the square of the $\eta$ parameter in the CKM matrix.

If we plug in the known values in CKM matrix, we get the branching ratio of $K_L^0 \to \pi^0 \nu\bar{\nu}$ as:

$$Br(K_L^0 \to \pi^0 \nu\bar{\nu}) = (2.49 \pm 0.39) \times 10^{-11}, \tag{1.13}$$

where the error is 71% due to uncertainties in the CKM matrix, 25% due to $X(x_t)$, and only 4% due to long distance uncertainties related to the matrix element [13].

## 1.2 Beyond the Standard Model

$K_L^0 \to \pi^0 \nu\bar{\nu}$ is an important probe of new physics beyond the Standard Model. The theoretical cleanness holds for virtually all extensions of the Standard Model.

$K_L^0 \to \pi^0 \nu\bar{\nu}$ happens at the loop level. This is part of the reason that makes the branching ratio so small. But the benefit is that the process is sensitive to new heavy particles since they could enter the loop diagram as virtual particles to alter the branching ratio.

$K_L^0 \to \pi^0 \nu\bar{\nu}$ is sensitive to the origin of CP violation. The branching ratio can be significantly larger with different CP violation origin. Table 1.2 lists the prediction of a few models. The three Minimal Flavour Violation(MFV) models give limited deviation from the Standard Model. They all assume that the CKM matrix is the only source for flavour

mixing. This made the CP violation origin in these models very similar to the Standard Model one. In the general Minimal Supersymmetric Standard Model(MSSM) and other models, the branching ratio of $K_L^0 \to \pi^0\nu\bar{\nu}$ can be 10 times larger.

| reference | $Br(K_L^0 \to \pi^0\nu\bar{\nu})/10^{-11}$ | model |
|---|---|---|
| [15] | a few $\times$ 10 | General MSSM |
| [16][17] | $31 \pm 10$ | Enhanced EW penguin |
| [18] | $< 4.6$ | MFV |
| [19] | $< 4.0$ | MFV w/ universal extra dimension |
| [20][21] | 3.1-6 | MFV w/ little-Higgs model |

Table 1.2: The predicted $K_L^0 \to \pi^0\nu\bar{\nu}$ branching ratios in some models beyond the Standard Model.

## 1.3 Experimental Status

There were efforts before our experiment searching for $K_L^0 \to \pi^0\nu\bar{\nu}$ [22][23]. E391a, our experiment, is the first dedicated experiment. The experiment was at the 12GeV proton synchrotron in High Energy Accelerator Research Organization(KEK). The E391a experiment started in February 2004 and had three data taking Runs(RunI, RunII and RunIII) ending December 2005.

We published the results of our first two runs(RunI and RunII) [24][25]. A combined upper limit on the branching ratio of $K_L^0 \to \pi^0\nu\bar{\nu}$ at the 90% confidence level was set as $6.8 \times 10^{-8}$.

This thesis describes the analysis of the last Run - RunIII.

# CHAPTER 2

# METHOD OF THE EXPERIMENT AND APPARATUS

$\pi^0$ in the final state of $K_L^0 \to \pi^0\nu\bar{\nu}$ decays into two photons 99% of the time. Since the two neutrinos are not visible to normal detectors, we can search for the decay $K_L^0 \to \pi^0\nu\bar{\nu}$ by looking for two photons with a transverse missing momentum($P_T$). The two photons are reconstructed into a $\pi^0$. The reconstructed $\pi^0$ $P_T$ and z are the two most important variables in the search. On the plane spanned by $P_T$ and the reconstructed $\pi^0$ z vertex, we use a simple rectangular box to select the $K_L^0 \to \pi^0\nu\bar{\nu}$ events. We call this box the signal box or the signal region. We show Figure 2.1 to illustrate the box(in red line).

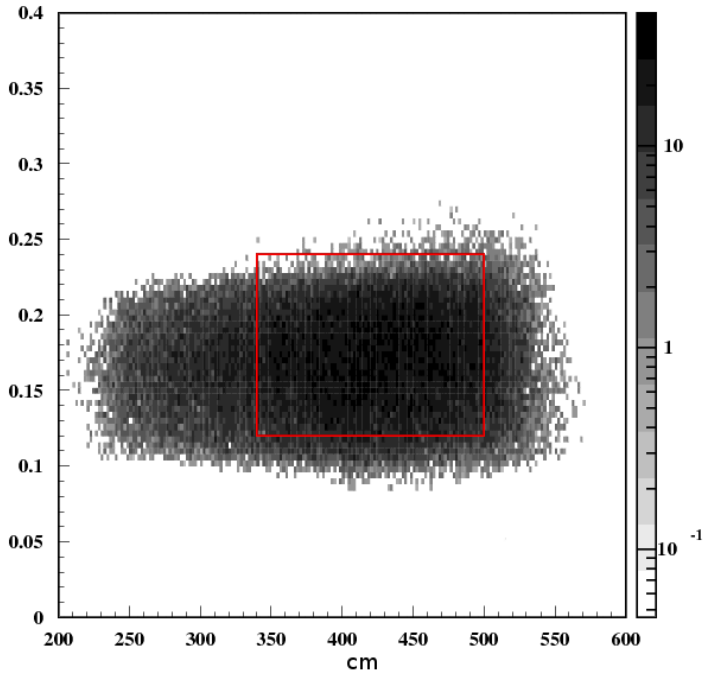


Figure 2.1: Illustration of the signal box(defined by the red lines) on the $P_T$ versus z plane. Potential $K_L^0 \to \pi^0\nu\bar{\nu}$ events are shown together with it.

To make sense of the search result(number of events found), we need to measure the total number of $K_L^0$'s which decays in our detector system(flux). Together with the probability

that a $K_L^0 \to \pi^0\nu\bar{\nu}$ decay will be success fully reconstructed and selected(acceptance or signal acceptance), the flux takes the search result into information on the branching ratio.

The other critical piece of measurement is the background estimation. We have to know if the events we find are $K_L^0 \to \pi^0\nu\bar{\nu}$ decay events or events caused by other physics processes. The signal box is designed to exclude as much background as possible while retaining the signal $K_L^0 \to \pi^0\nu\bar{\nu}$ events. Our choice will be clear in Chapter 5.

To avoid human bias, we adopted a blind analysis approach. We didn't look into the signal box region in data until we finished all the analysis work except for looking at what we got in the signal box(open the box).

To make these measurements we need to have lots of $K_L^0$'s and a detector system that detects all the particles in an event. In this chapter we will discuss the hardwares for these purposes including the beamline which produces and collimates the $K_L^0$ beam, the detector system and the data acquisition system. We will also describe how we reconstruct photon, $\pi^0$ and $K_L^0$ from the raw detector activities.

## 2.1 The Pencil Beam

In the E391a experiment, $K_L$'s were produced by 12 GeV protons from KEK-PS hitting a platinum target. We need a narrow and well-collimated beam. This is important because the only information about the signal event $K_L^0 \to \pi^0\nu\bar{\nu}$ is the energy and position of the two photons. We need to assume the $\pi^0$'s were from the beam axis to reconstruct the events and to find the key signature of the signal: $P_T$. The pencil beam is also essential for background control. The interaction of particles with off-axis material is the dominant background source as shown later in Chapter 5.

Our beamline was made of two sweeping magnet, six heavy metal collimators, two absorbers and a vacuum pipe. The last collimator was called C6. It was located 2 meters

upstream of our detector.

The average $K_L^0$ momentum at the exit of the beamline was 3 GeV/c. The beam core had a half cone dispersion of 2 mrad. There are about 60 times more neutrons than $K_L^0$ in the beam. The distribution of neutron x-axis projection at the z position 6 meters downstream from the exit of the beamline is shown in Figure 2.2. More details of the beamline can be found in [26].

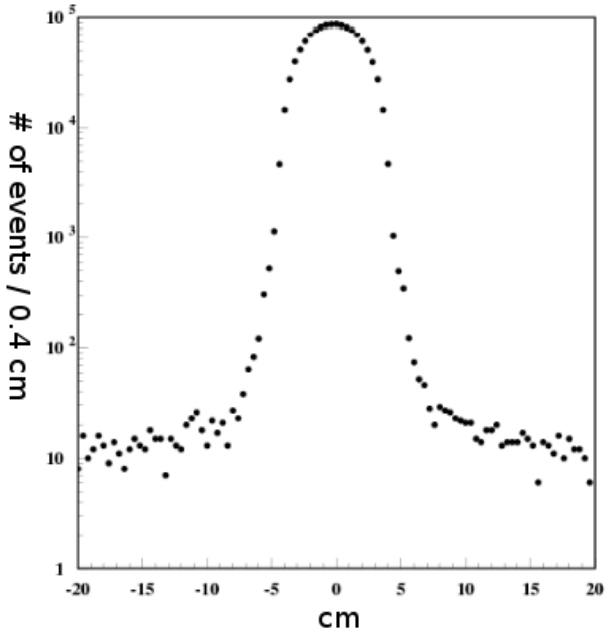


Figure 2.2: The distribution of neutron x-axis projection at the z position 6 meters downstream from the exit of the beamline. This distribution is important because it is the input for the background simulation.

## 2.2 Hermetic Veto and Calorimeter System

Figure 2.3 shows the cross-sectional view of the E391a detector. The beam came from the left on the figure. The region that we cared the most was called the decay region, or the fiducial region. It was the main chamber in the Main Barrel and between CsI and FB.

Figure 2.4 is a cartoon of the E391a Detector to visualize what the whole detector looks

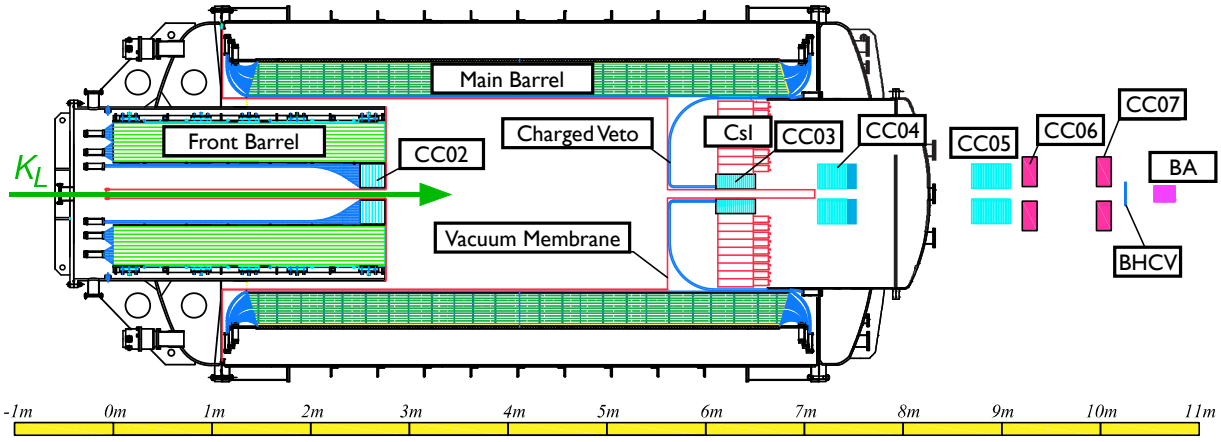


Figure 2.3: The E391a Detector cross section view. We define a coordinate system as follows. The origin is at the beginning of the detector system. The $z$-axis points downstream and the $y$-axis points vertically upwards. This is the coordinate system that is used throughout this thesis. It will be often used in the reconstruction plots.

like.

### *2.2.1 The Calorimeter*

The most important subsection was the main calorimeter. It was mainly made of cesium iodide(CsI) crystals. This inorganic crystal scintillator have a good energy resolution.

The main calorimeter formed a round disk with a diameter of 2 meters at the end of the decay region. It was made of 576 blocks of CsI crystal. The most inner 24 blocks were $5cm \times 5cm \times 50cm (= 27$ radiation length$(X_0))$. The rest, which were the majority, had a dimension of $7cm \times 7cm \times 30cm (= 16X_0)$. We attached different photo-multiplier tubes(PMT) at the end of the crystals according to their size.

Obviously, squares won't fill out a circle perfectly. We reduced the gap at the outer edge by cutting crystals and filling in additional lead/scintillator sandwich-"Sandwich Modules"(SAND). The layout is shown in Figure 2.5.

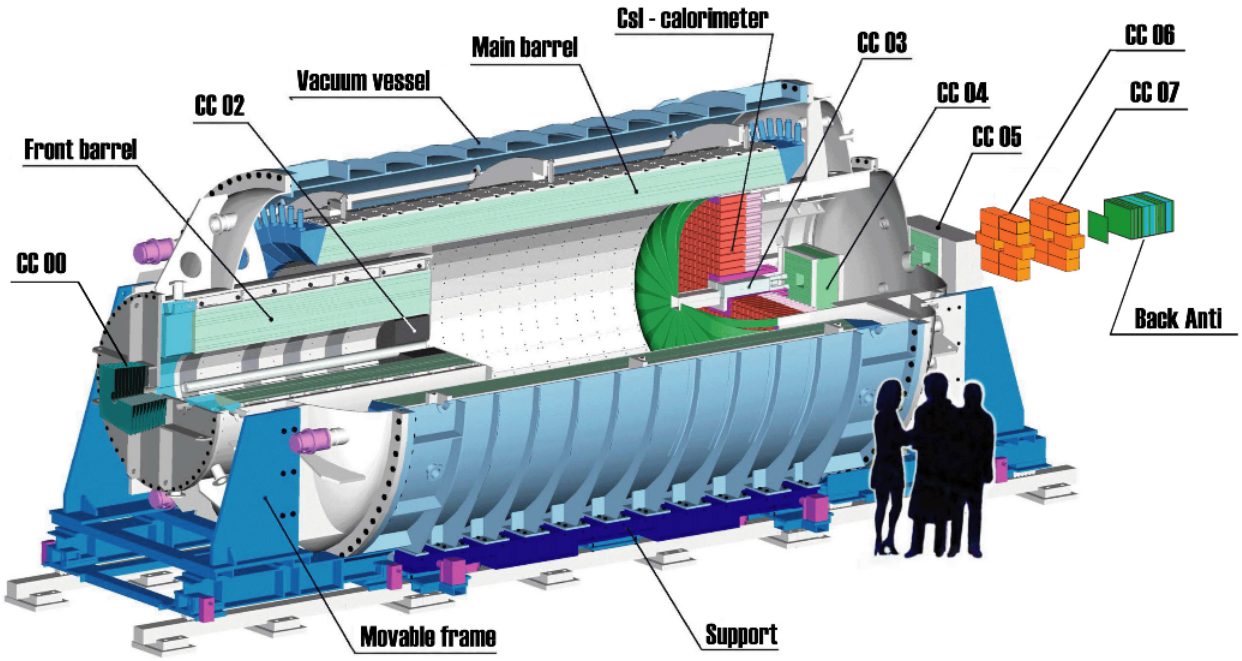


Figure 2.4: The full E391a Detector.

### *2.2.2 The Charged Veto*

The plastic scintillator in front of CsI was our main Charged Veto(CV). We placed it 50cm away from CsI. To read the scintillator light out, we bent the plastic plates to surround the outer edge of CsI, and connected them to PMT outside of the decay volume. The CV was grouped into the outer CV(OCV) and the inner CV(ICV). The OCV had 32 plastic scintillator plates. The ICV had four plastic scintillator plates around the beam between OCV and CsI. The thickness of all scintillators was 0.6cm. See Figure 2.6 for an illustration.

### *2.2.3 The Barrel System*

The main photon veto was called Main Barrel(MB), shown in Figure 2.7. It caught most of the extra particles. MB was 5.5 m in length, 2.00 m in inner diameter, and 2.76 m in outer diameter. It was made of 45 layers of lead and plastic scintillator. The total thickness was

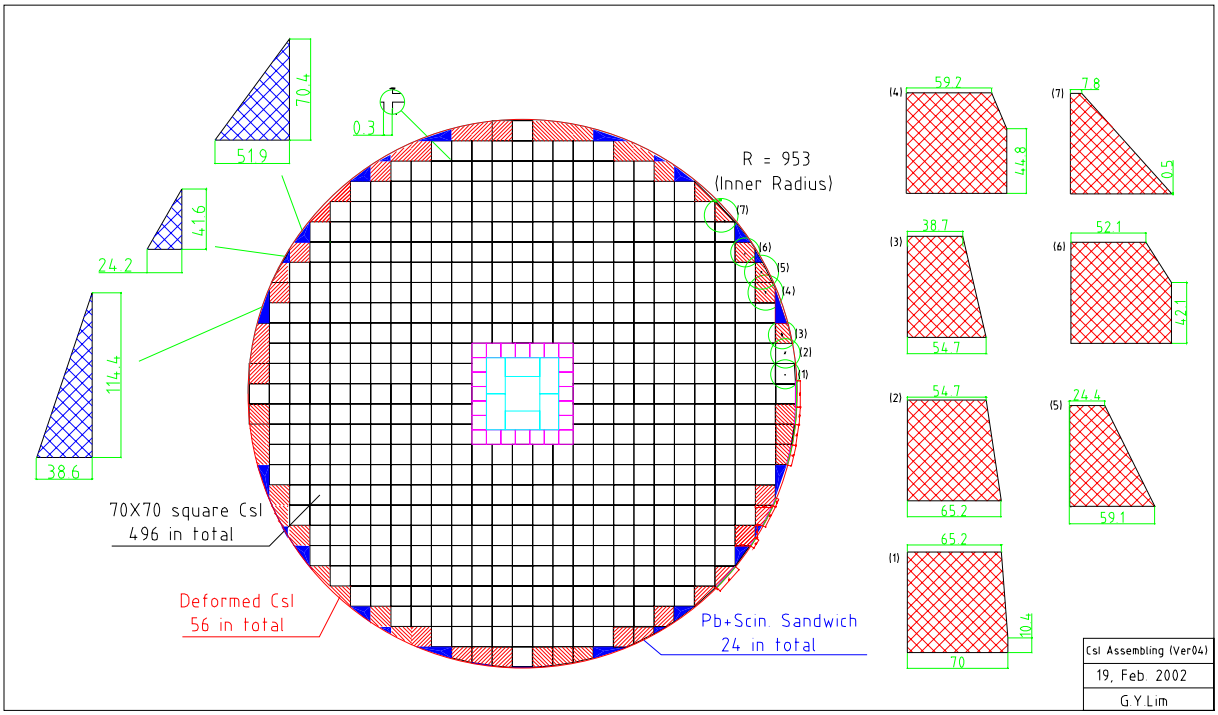


Figure 2.5: The components of the outer edge of the CsI array. The Sandwich Counter modules are the triangular blocks. They were built from lead and plastic scintillator plates, oriented parallel to the beam. There were a total of 24 such counters, grouped into eight groups of three for readout purposes. The deformed CsI blocks were each read-out individually.

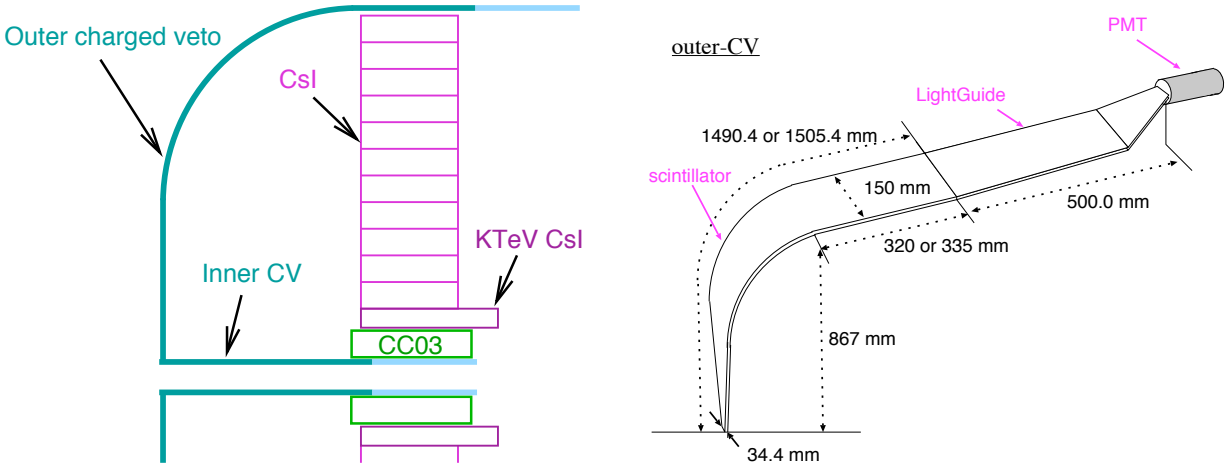


Figure 2.6: The Charged Veto (OCV).

$13.5X_0$. There were 32 modules. Each of them was a trapezoid as in Figure 2.8. Wavelength-shifter(WLS) fibers were used to read out the scintillator light. WLS fibers reduced the light attenuation effect in the long scintillator plates. They had an attenuation length of 450cm comparing with the 45cm attenuation length of the plastic scintillator. The fibers were extended to both ends of each module. At each end, the fibers from different layers of scintillator were grouped into two bundles(inner and outer) and connected to PMTs. So altogether, we had 128 PMTs, or 128 readout channels for MB.

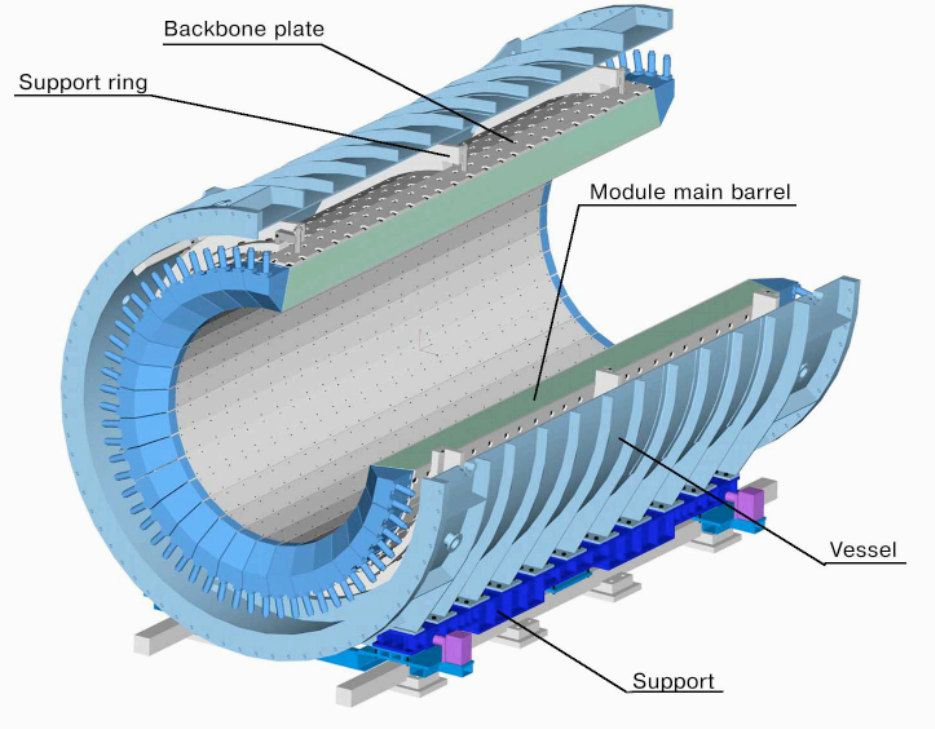


Figure 2.7: The Main Barrel and vacuum tank.

Right next to the most inner layer of MB, we also placed a scintillator detector with readout on it to reject charged particles more effectively.

The other smaller barrel-like detector was Front Barrel(FB). FB had 16 modules. It was 2.75 m in length, 0.62 m in inner diameter, and 1.45 m in outer diameter. Its thickness was equivalent to 17.2 radiation length.

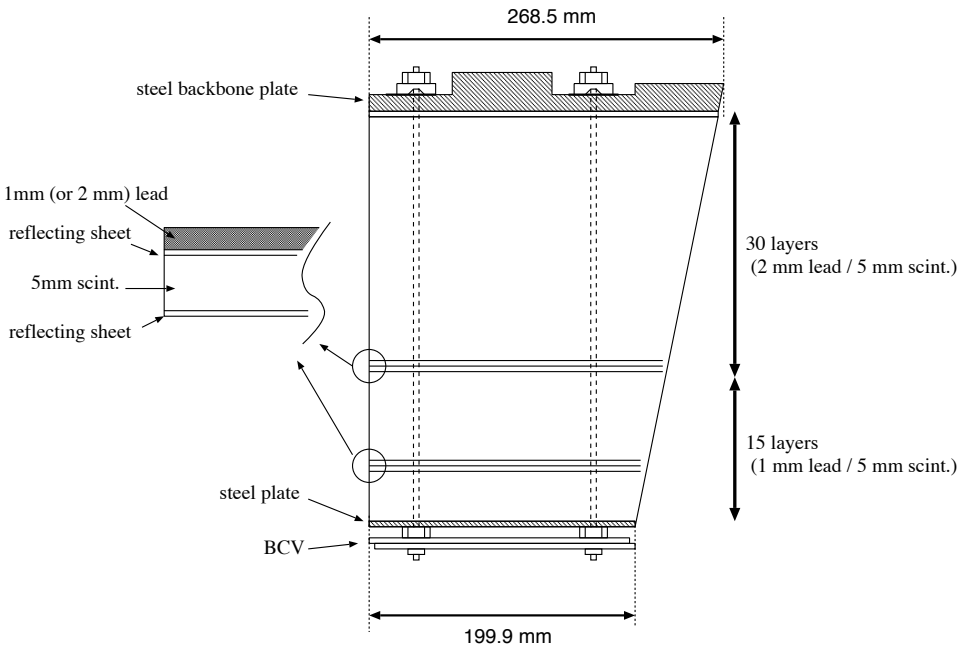


Figure 2.8: A single Main Barrel module.

We only had readout on one end of FB. We didn't place PMT inside the decay region to read out the downstream end to keep the decay region as clean as possible. Instead we aluminized that end to have the light reflected to the front end, and used PMT to read it out at that end. The light yield varied from 10 to 20 photo-electrons per MeV energy deposit depending on the distance from the hit point to PMT.

### *2.2.4 Collar Counters*

There were seven Collar Counters(CC') surrounding the beam at different z position. They were labeled as CC00, and CC02{2-7} from upstream to downstream.

CC02 was essential to form the $4\pi$ hermetic veto coverage. It was located inside FB, and at the downstream edge of FB. There were 8 octagonal modules in CC02. Each module was made of lead and plastic scintillator layers. Inner beam hole was 15.84cm in diameter. Its shape and dimension are shown in Figure 2.9. The total radiation length was $15.73X_0$. The

light yield was around 10 photo-electrons per MeV.

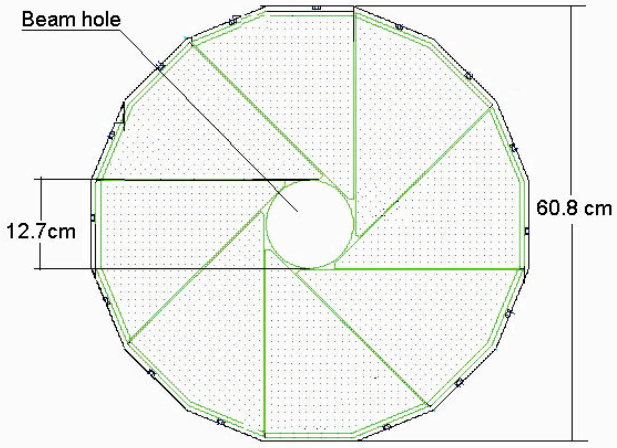


Figure 2.9: CC02, shown here looking downstream (the beam would pass through the center gap region).

CC03, shown in Figure 2.10, was located at the center of the Main Calorimeter. Instead of lead/scintillator sandwiched layers, it was made of tungsten/scintillator layers.

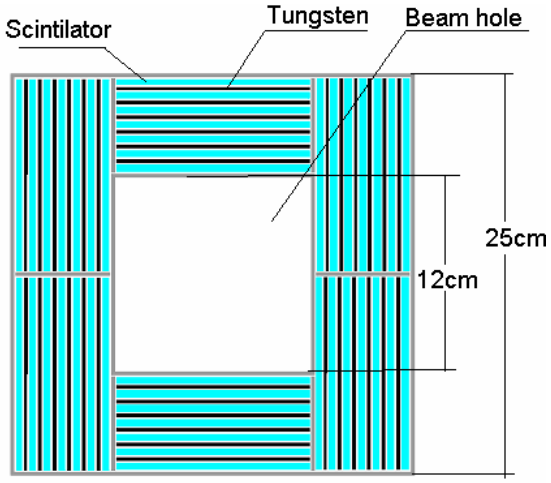


Figure 2.10: CC03 as seen looking down the beam axis.

There were four of downstream collar counters behind CsI: CC04, CC05, CC06, and CC07. CC04 and CC05 were lead/scintillator sandwiched layer detectors. CC06 and CC07 were made of lead glass blocks. See Figure 2.11 and 2.12 for the layouts. More detailed

information is in [27].

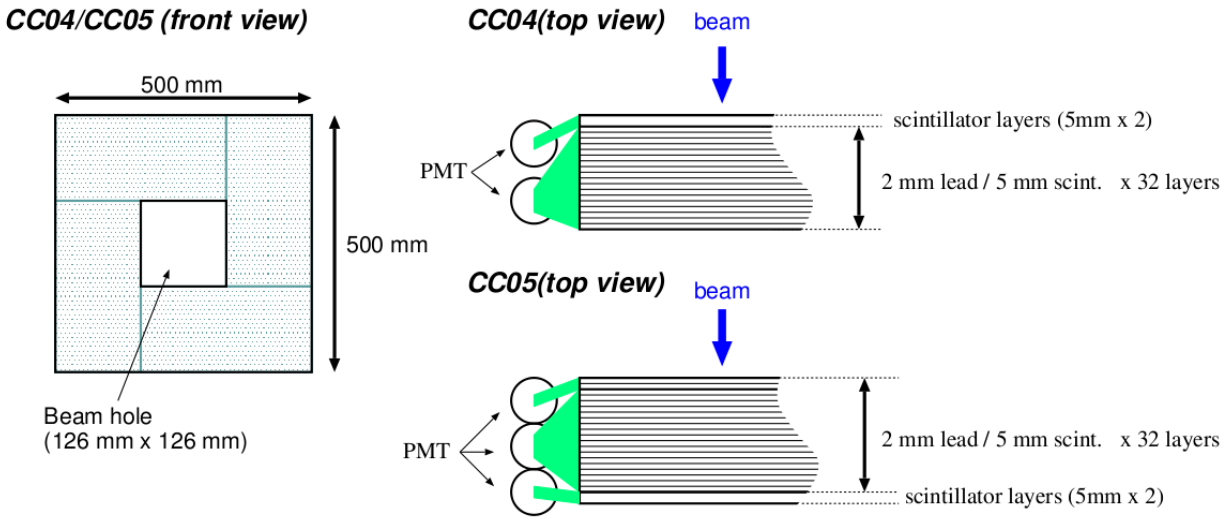


Figure 2.11: CC04/CC05 - both detectors were constructed almost identically out of lead-scintillator layers. CC05 had charged veto layers(single scintillator layer) on both ends while CC04 had it only on the side facing CsI(upstream).

Since RunII, we had also installed CC00 between the end of the beamline and the start of the detector system. It was made of tungsten/plastic scintillator sandwiched layers.

### *2.2.5 The Beam Anti and the Beam Hole Charged Veto*

At the end of beam pipe we had a special photon veto detector called beam anti(BA). BA was subject to a high intensity of beam. If we had vetoed everything as in other veto detector, we would have lost much of our acceptance. So BA must discriminate photons against the majority particles in the beam - neutrons.

We achieved this purpose by using a Cerenkov light detector, quartz. Charged particles in quartz must have a velocity of $\beta > 1/n$ to give out Cerenkov light. There are much smaller number of particles in the hadronic shower of neutron to satisfy this condition comparing with the number of electrons and positrons in the electromagnetic shower of photons.

BA was made of 5 layers of quartz and 5 layers of PWO crystals. PWO served the

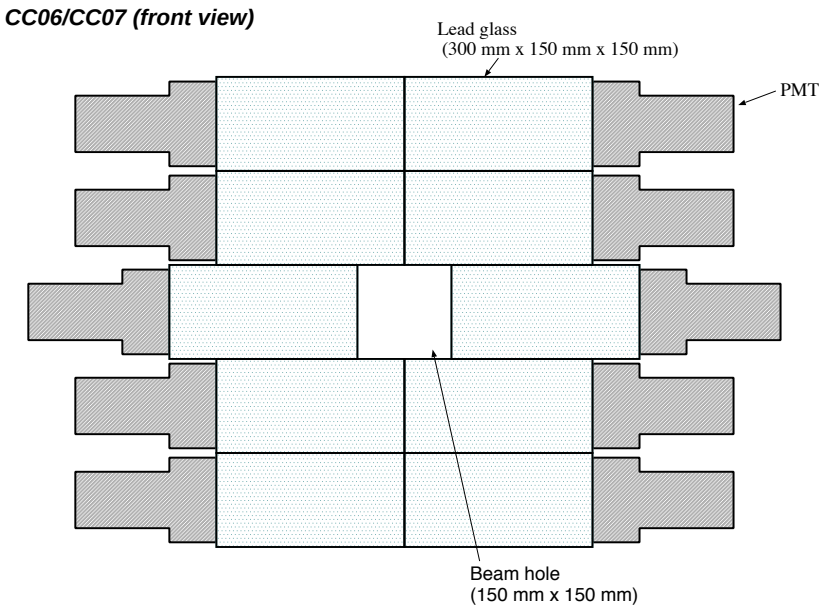


Figure 2.12: CC06/CC07 - both detectors were constructed identically out of lead-glass blocks.

purpose of showering and photon veto. Each crystal was wrapped individually. There were 80 readout channels for PWO and 35 for quartz.

We also had 8 pieces of plastic scintillators in front of BA. The thickness of them was 0.3 cm. Although this detector was in the beam, it wouldn't be set off by neutrons. So we could apply a simple veto to get rid of charged particles.

### *2.2.6 The Vacuum System*

Interactions of neutrons with air can give us background. So we want to keep it as clean as possible in the decay region. We managed to achieve $10^{-5}Pa(8 \times 10^{-8}$ torr) of high vacuum in the decay region. This suppressed the background from neutron-air interaction to be $< 0.001$ at E391a sensitivity.

Due to the out-gassing of the giant detector system, we had to adopt a two-stage vacuum system. A thin film was used to separate the decay region and the detectors. The decay

region was in the high vacuum of $10^{-5}Pa$. The film separating the detectors and the decay region were thin($190\mu m$, $0.0004X_0$) to avoid absorbing particles. This made it vulnerable to excessive pressure. We reduced the pressure on the film by keeping a vacuum of 0.1 Pa in the detector region. The vacuum system is shown in Figure 2.13.

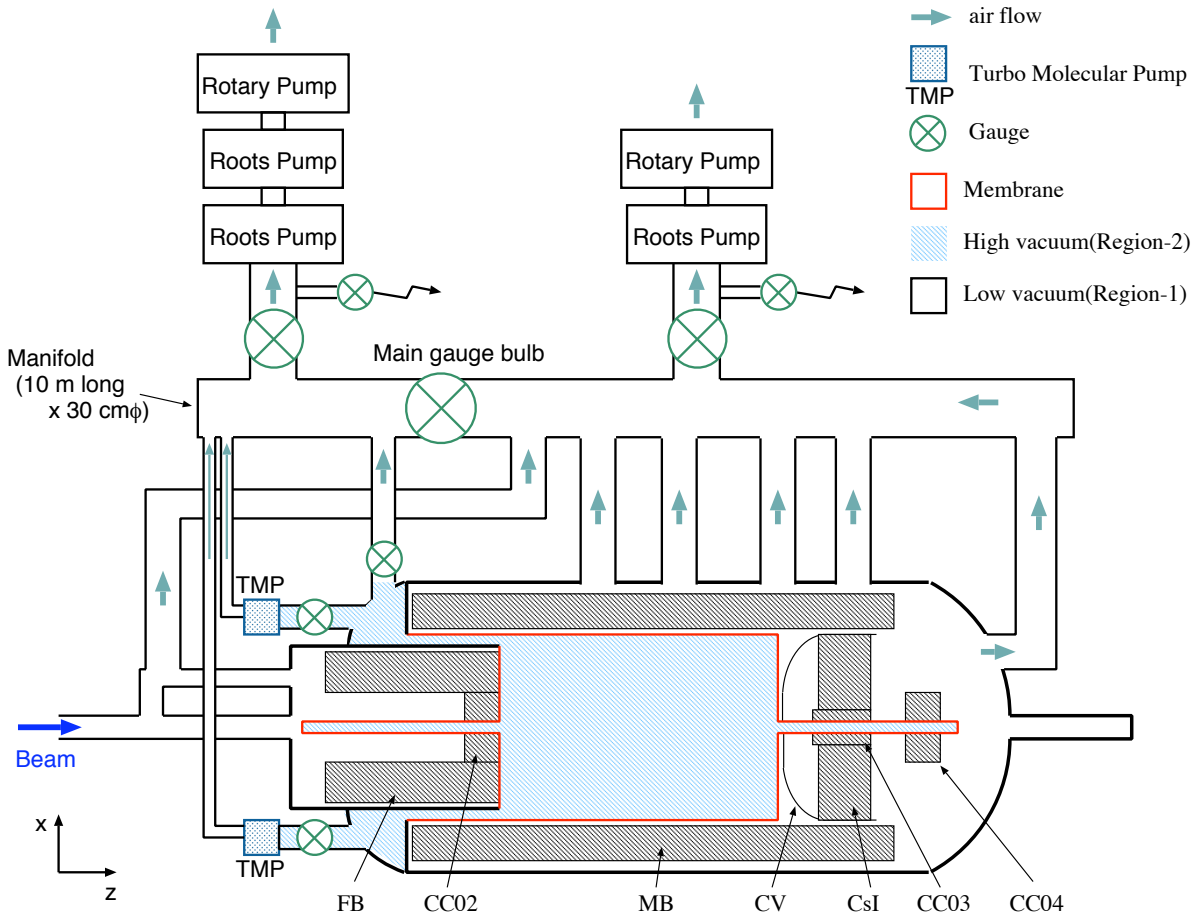


Figure 2.13: The vacuum system.

The vacuum in the detector region could cause a heat dissipation problem, especially for CsI. We ran cool water in copper pipe at the back of CsI. Heat conduction wires were connected to the PMT. During the data taking, we monitored the temperature at CsI and PMT. It was stable around 20 degree Celsius. For more technical details please refer to [28].

## 2.3 DAQ Electronics

All E391a detectors were connected to PMTs. The PMT signals after the Amplifier-Discriminator (AD) modules were digitized by analog-to-digital converters (ADC's). They were also transmitted to time-to-digital converters (TDC's). The energy and time information from the ADC's and TDC's were read out by Fastbus-VME system. We saved the energy and time information for every detector channel in our experiment. We had about 1000 Chanel's in our detector. And the data size was around 10Kbytes for one event.

The bottleneck of this system was the LeCroy 1885N FASTBUS ADC charge conversion time, which was 750 microseconds.

Further details on the DAQ are available in [28].

## 2.4 Trigger

To keep our data acquisition system working efficiently, which was to take the interesting data as much as possible, we needed to cut down on the event rate while trig the DAQ system on the potential $K_L^0 \to \pi^0\nu\bar{\nu}$ event. We found the following condition satisfying our requirement.

In the main calorimeter, we divided the signals from 576 blocks of CsI crystals into 72 bundles of eight, forming hardware clusters(HWC). The eight crystals in one bundle were all neighbors in the CsI stack. Our physics trigger required two or more HWC's, with an energy threshold of 80 MeV. Later in the final analysis, we adopted a photon minimum energy requirement tighter than this.

We further reduced the event rate with online veto selection. We set a loose threshold just to keep the rate low enough. As with the HWC selection, we imposed tighter selection later in the offline analysis. We did not use the detectors in the beam for online to avoid false veto.

With our setting, the physics trigger rate was about 180 Hz. Together with 30 Hz of accidental and minimum bias triggers, we had a DAQ live time of about 90% for RunIII.

One can see that we were not only targeting our trigger at $K_L^0 \to \pi^0\nu\bar{\nu}$. Neutral $K_L^0$ decay were all recorded if all daughter particles ended up in CsI. Events could also be recorded if there were particles ended up in the veto detectors, but the veto activity was below the veto threshold. This is important for us to collect the data to figure out the total number of $K_L^0$(flux).

We also had triggers for the purpose of accidental data collecting, detector calibration and even special runs where we had different conditions and purposes. They will be covered when they are used in the later chapters.

## 2.5 Event Reconstruction

The E391 experiment looked for signal $K_L^0 \to \pi^0\nu\bar{\nu}$ and normalization mode($K_L^0 \to 3\pi^0$, $K_L^0 \to \gamma\gamma$, and $K_L^0 \to \pi^0\pi^0$) by using photons from the $\pi^0$ decays. Comparing with experiments using the charged decay of $\pi^0$'s, we gain by having the 99% of $\pi^0$ decay branching ratio. But we also lose by not knowing the decay vertex from charged particle tracking. We will describe photon finding, photon reconstruction and $K_L^0$ and $\pi^0$ reconstruction in this section.

### *2.5.1 Photon Finding*

The first step was to connect the neighboring CsI crystals with energy deposition together. The detail of the algorithm is shown below:

- First we compile two lists. One list contains all crystals with 5 MeV or more energy deposited(seed crystal). The other list have all crystals with energy over 1 MeV.

- Then, we define a cluster by the crystal with the largest energy deposited in the seed crystal list, we add crystals to the cluster by including every neighbor from the two lists. Here neighbors are defined to be crystals that shared an edge. Once one crystal is added to the cluster, its neighbors are searched in the two lists. When we add one crystal to the cluster we also delete it from the lists we've compiled in the first step.

- When there is no more neighbors to any of the cluster crystals in the two list, we go back to the last step, start with the next highest energy deposited crystal the crystal from the list of remaining seed, and repeat the above process.

- After all the seeds have been used, we do a first stage fusion event cut. If two photons hit the CsI calorimeter with a good separation, but their clusters are connected, two local maxima are usually found in the cluster, where a local maximum is defined as a crystal with energy higher than all four of its neighbors.

- It is worth to mention that not all crystals with energy deposition will be covered by clusters. We require the number of crystals in the cluster to be at least 2. Crystals with energy below the seed threshold and seeds without neighbors are classified as "single-hit" crystals. Many single-hit crystals are found on the diagonals of good clusters and are an artifact of the clustering algorithm. Others are due to very soft photon interactions. The Molliere radius in CsI is about 3.5 cm. The width of most of the crystals is 7 cm. As a consequence, some electromagnetic showers are completely contained by single crystals. Finally, some single-hit crystals are due to other particles. The single-hit crystal energy deposition is used as a veto.

### *2.5.2 Photon Reconstruction*

The most naive and direct position and energy information about the photon from the cluster is the center of energy position of the cluster and the total energy deposition in the cluster. Due to shower leakage and the incident angle dependence of photon shower, these values deviate from the true information. We improved the photon reconstruction by making corrections relying on simulation.

We simulated photons with a variety of angles and energies using GEANT4 MC [29]. Knowing the incident photon position or energy, we inferred the other by using a table we made by MC. The detail about the construction of this table can be found in [30].

One can see that this correction procedure is a iterative process. We fed the photon angle information from the $K_L^0$ and $\pi^0$ reconstruction in addition to the center of energy position and total energy deposition to the correction table to get a better photon position and energy measurement. We improved by feeding the updated angle and energy information each time. Typically, the correction converged within three iterations.

The correction tables improved the photon hit position resolution (the Gaussian width of the distribution of true position minus reconstructed position) from 2.6 cm to 1.1 cm, the energy bias from 20.7 MeV to -5.7 MeV, and the $\pi^0$ vertex resolution from 8.9 cm to 6.6 cm, as displayed in Figure 2.14 [30].

### *2.5.3 $\pi^0$ and $K_L^0$ Reconstruction*

We reconstructed a $\pi^0$ from two photon without the photon direction information. This was possible because of our pencil beam feature. We always took the x,y position of the $\pi^0$ decay

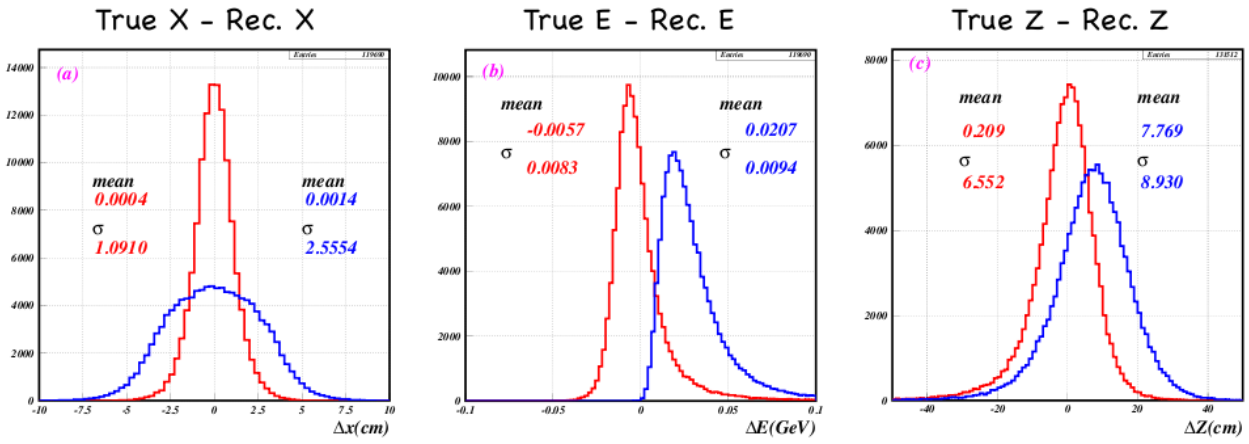


Figure 2.14: Before (blue) and after (red) the energy and position correction routines as applied to (a) the photon hit position (in $x$), (b) the photon energy, and (c) the $\pi^0$ $z$-vertex. "True - Rec." means the known true MC value minus the reconstructed value. The associated means and widths (RMS) for the corrected clusters are displayed on the left side of each sub-figure, while the original center-of-gravity calculations are provided on the right side of each sub-figure.

vertex at 0's. The only unknown variable:z position was backed out from the $\pi^0$ mass:

$$\begin{aligned} m_\pi^2 &= (p_1 + p_2)^2 \\ &= p_1 p_1 + p_2 p_2 + 2 \times p_1 p_2 \\ &= 2 \times (E_1 E_2 - \mathbf{p_1} \cdot \mathbf{p_2}) \\ &= 2 E_1 E_2 \, (1 - \cos\theta) \end{aligned} \tag{2.1}$$

$$\begin{aligned} r_{12}^2 &= d_1^2 + d_2^2 - 2 d_1 d_2 \times \cos\theta \\ d_1^2 &= r_1^2 + (z - z_{CsI})^2 \\ d_2^2 &= r_2^2 + (z - z_{CsI})^2 \end{aligned} \tag{2.2}$$

where $p_i$ is the four momentum for the $i$-th photon, $\mathbf{p_i}$ is the three momentum for the $i$-th photon, $E_i$ is the energy for the $i$-th photon, $r_{12}$ is the distance of the two photon hitting

position on the CsI face, $d_i$ is the distance from the photon CsI hitting position to the z axis, $z$ is the decay vertex z position, $\theta$ is the angle between the two photon directions, and $z_{CsI}$ is the z position of the CsI front face, which is 614.8cm in our definition. See Figure 2.15 for an illustration of the reconstruction. Note that for $K_L^0 \to \gamma\gamma$ events, we simply replaced the $\pi^0$ mass with the $K_L^0$ mass in this equation.

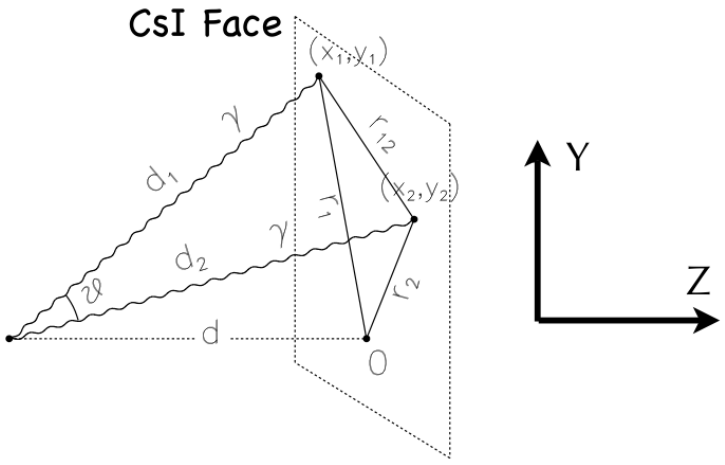


Figure 2.15: A diagrammatic representation of $\pi^0$ reconstruction according to Equation 2.1 and 2.2.

After we reconstructed $\pi^0$'s from pairs of photons, the main hurdle to reconstruct $K_L^0$ for $K_L^0 \to 3\pi^0$ and $K_L^0 \to \pi^0\pi^0$ was that there are multiple ways to make pairs of photons for $\pi^0$ reconstruction. There are 15 different combinations to make pairs of photons for $K_L^0 \to 3\pi^0$, and there are 3 for $K_L^0 \to \pi^0\pi^0$. Figure 2.16 is a cartoon showing the $K_L^0 \to 3\pi^0$ reconstruction for one combination.

$\pi^0$'s can only travel less than one micron at our energy level. This is far smaller than our position resolution( cm) and the z vertex differences of $\pi^0$'s at wrong combinations( 10cm-1m). So the vertices of $\pi^0$'s in the reconstruction should be close to each other. We used the differences of the $\pi^0$ vertices to determine if the combination was the right one.

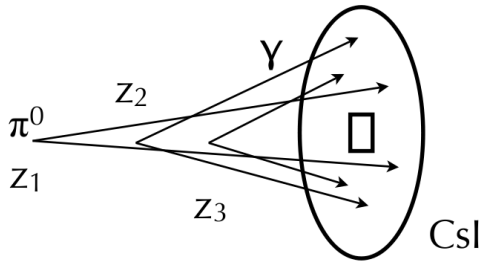


Figure 2.16: A diagrammatic representation of $K_L^0 \to 3\pi^0$ reconstruction, where each $\pi^0$ is first reconstructed according to Figure 2.15.

In practice, the differences of the $\pi^0$ z vertices was defined as:

$$\begin{aligned} \chi^2 &= \sum_{i=1}^{n} \frac{(z_i - \bar{z})^2}{\sigma_i^2}, \\ \bar{z} &= \frac{\sum_{i=1}^{n} z_i/\sigma_i^2}{\sum_{i=1}^{n} 1/\sigma_i^2}, \end{aligned} \tag{2.3}$$

where $n = 2$ for $K_L^0 \to \pi^0\pi^0$ and 3 for $K_L^0 \to 3\pi^0$, $z_i$ is the $i$-th $\pi^0$ reconstructed z position, and $\sigma$ is the result of error propagation on the uncertainty in the energy and position through Equation 2.1 and 2.2.

The lowest-$\chi^2$ solution was our preferred solution. In order to discriminate against cases where two solutions were close together and the correct solution might have fluctuated to the higher value of $\chi^2$, we also cut the events with small second best $\chi^2$ values.

# CHAPTER 3

# DETECTOR CALIBRATION

In general, the energy calibration of different detectors were done by using cosmic or beam muons during the special muon runs. In this chapter I show the CsI calibration and the CV inefficiency study, which I worked on. The CV inefficiency study was pioneered in RunIII analysis. For the calibration of other detectors, please refer to [31] and [27].

## 3.1 CsI

CsI is the most important detector. We need to know how to use it to measure photon energy. There were several procedures we did before and during the data taking.

The linearity was tested using electron beams in the energy range of 0.5-3.0 GeV, which our photons expected to be in [32]. We found the PMT readout was in a very good linear relation with the energy of the incident beam particles. So we only needed one parameter-the gain factor for the calibration. We determined the gain factor in two steps.

In the first step to measure the gain factor, we used the minimum ionization peak by cosmic muons. Muons leave 5.63 MeV of energy in CsI for every cm of traveling length. This is true for a wide range of muon energy. The key of the calibration in this step was to find the muon track with our detector setup. The granularity of CsI enabled us to do this. We first selected cosmic events by requiring the coincidence of opposite MB modules in the trigger. A line was then fitted through the track crystals using least-squares fit in the (x,y) plane. Muons won't produce wide-spread shower and will just leave energy in the CsI blocks on or close to its track. So the fitting $\chi^2$, measuring the deviation of cluster from a line, can be used for selecting muon tracks. We also required the track to be at least 70cm in length to get good muon tracks. The length of tracks going through CC03 and the beam hole was

calculated by using the sum of track length on the two sides. The path length of the cosmic muon in each block was found once we had the track orientation fitted [32].

Because we didn't have granularity in the z direction, the path length we could not get the z projection of the path length. We reduced this effect by selecting longer track in the (x,y) plane. But it was still not a precise calibration.

To improve this, we used the kinematic constraints in $K_L^0 \to 3\pi^0$ to refine the calibration [33]. The six kinematic constraints in $K_L^0 \to 3\pi^0$ are:

- $M_{6\gamma} = M_{K_L}$
- $M_{\gamma\gamma} = M_{\pi^0}$ $(\times 3)$
- $\sum_i (x_i \times E_i) = v_x \times \sum_i E_i$
- $\sum_i (y_i \times E_i) = v_y \times \sum_i E_i$

These six equations relies on six photons' $(x, y)$ position and energy, $E$. There is also an assumption that the transverse momentum of $K_L^0$ is zero. There are three unknowns to solve for - the vertex of the $K_L^0$ decay.

A least-square fit can be found for this system by Lagrange multipliers with three degrees of freedom. The fitting process also uses our understanding of the uncertainties on the photon position and energy.

To use these constraints to calibrate, we floated the energy of one cluster. The fit gave us the energy of that photon in addition to the $K_L^0$ vertex. The ratio between the measured and calculated energies was used to correct the gain of the CsI crystals. It took around four iteration to converge. We used this procedure to calibrate the crystals in all six photon clusters. The correction ratios for the same crystal in different events were averaged.

It took about one shift(8 hours) worth of data to get enough hits for the edge crystals,

where there were much less hits. So roughly speaking, we refined the calibration independently for every shift.

The improvement of CsI gain is shown in terms of $K_L^0$ and $\pi^0$ mass width in Figure 3.1

This calibration method only adjusted relative gains among the 576 CsI crystals. It reduced 576 unknowns down to 1, which was the overall absolute energy scale. We used the $\pi^0$'s produced at CC02 by halo neutrons to check the absolute energy scale. We show the halo neutron Monte Carlo results in Chapter 5, where the z vertex of CC02 events is at the same place as in data. This confirms that the absolute energy scale was correct.

## 3.2 CV

The importance of CV is to veto events of charged decays by $K_L^0$. Inefficiency of CV is the probability that CV will miss a charged particle. The inefficiency of plastic scintillator(CV) was measured before our experiment [34]. To be sure that we didn't have a crack or electronics failure in this important veto after installation, we also performed the check of photon veto inefficiency during data taking to make sure that we didn't miss charged particles in the detector system.

Just using data in muon run for this purpose is not enough. We don't just need lots of muons, we also need a clean muon sample. To clean the data sample and identify a muon, we used our CsI array. If the energy deposition in one block of CsI is around the minimum ionization peak( 200MeV for 30cm long CsI and 350MeV for 50cm long CsI), the neighboring CsI blocks will also have energy deposited for hits caused by most particles. By requiring a single hit in the CsI array and veto on CC03, we selected clean muon sample in the muon runs.

In addition we vetoed on the collar counter in the middle of the calorimeter-CC03 to avoid showers spreading into CC03. We also required coincidence with CC02 in addition to

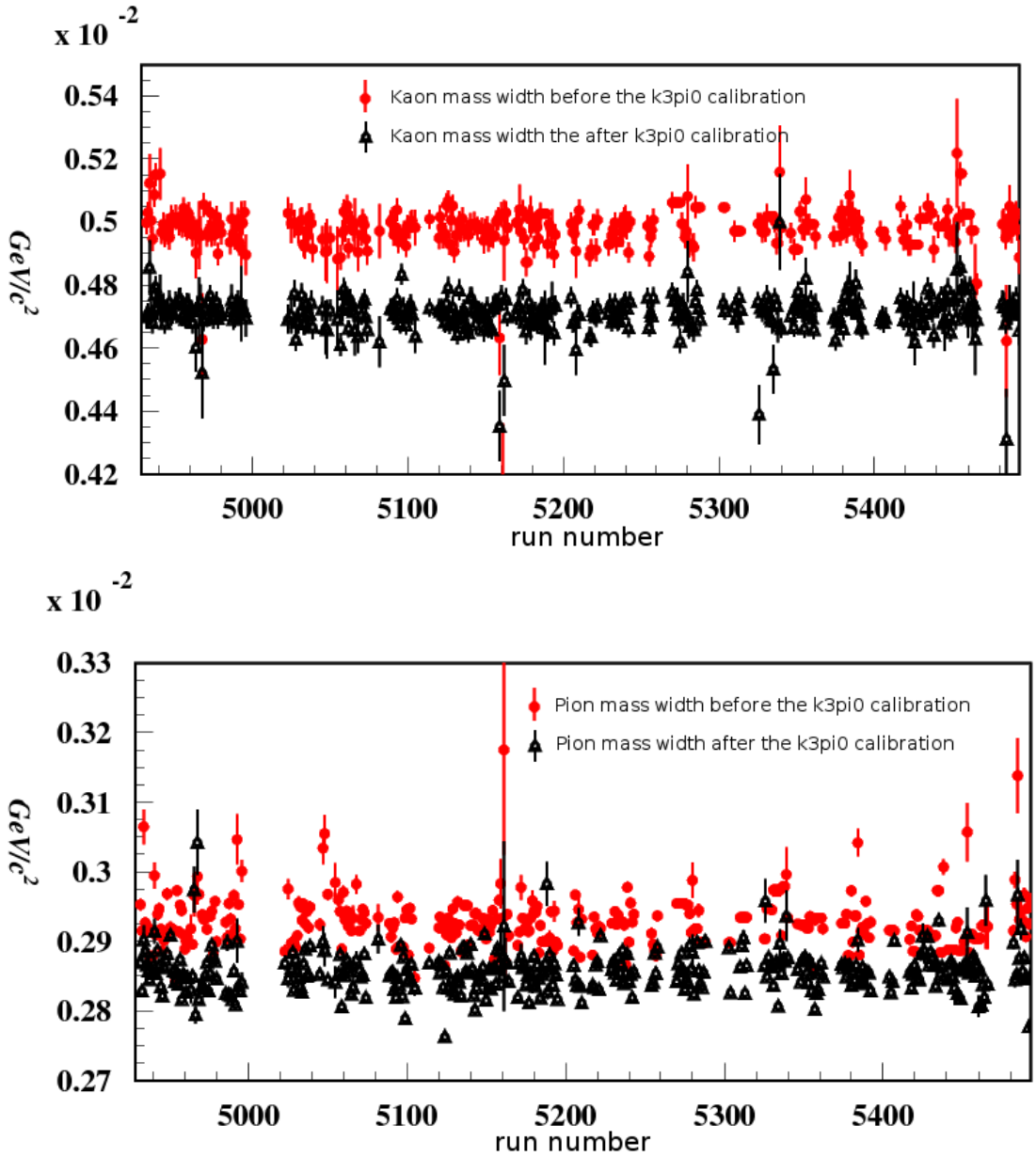


Figure 3.1: The mass width of $K_L^0$ and $\pi^0$ in each individual run. The run number ranging from 4932 to 5472 is on the horizontal axis. The outliers on these plots correspond to small runs. Note that "run" is different from "Run" as in "RunIII". The former one is 2 hours of data taking period we used to keep the data file size reasonable.

CsI hit.

The CV energy deposition in the selected sample, shown in Figure 3.2, confirmed that particles going through was all($> 99.999\%$) charged particles(muons) and the CV worked fine without crack of electronics failure. The "inefficiency" that we can get from this plot is $1.3 \times 10^{-5}$. As we will show in Chapter 5, an inefficiency of $10^{-4}$ is enough to suppress all $K_L^0$ charged mode decay backgrounds.

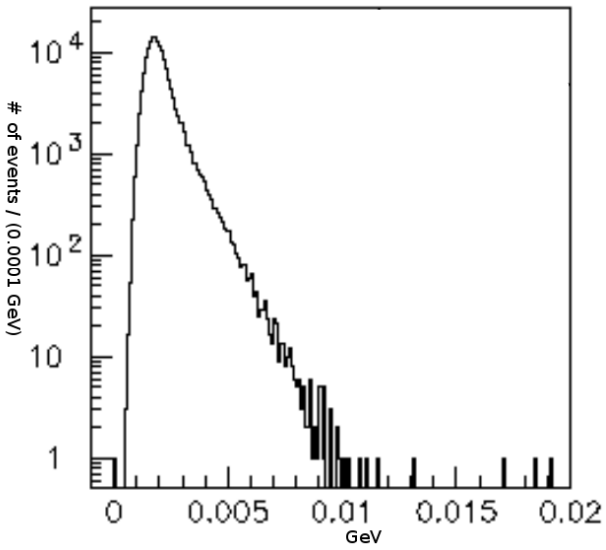


Figure 3.2: Energy deposition in CV with muon tag defined by the condition set in the text.

In this study the photon veto inefficiency should be considered as the probability of leaving energy below the threshold when muons pass through the scintillator.

# CHAPTER 4

# $K_L^0$ MONTE CARLO AND FLUX NORMALIZATION

After the detectors were calibrated, one of the first things that we wanted to know is the behavior of $K_L^0$. In other words, we need a reliable $K_L^0$ Monte Carlo(MC) simulation to calculate the total number of $K_L^0$(flux) and the fraction that we can reconstruct and accept for each decay mode(acceptance). In this chapter we describe the $K_L^0$ MC and the $K_L^0$ flux calculation. The $K_L^0 \to \pi^0\nu\bar{\nu}$ acceptance is shown in Chapter 5 together with the final result.

## 4.1 $K_L^0$ Beam Profile

We chose the exit of collimator system as the starting point of simulation. $K_L^0$ was generated according to distributions of its kinematic variables, namely momentum and radial position. But the spectrum of these variables that we observed in data was always convoluted with the acceptance. To fit $K_L^0$ beam profile, we took an iterative approach.

After many iterations of tuning, we found that the radial position distribution of data and MC didn't match well. We had to apply an event weight based on the radial position. The weight function is defined as:

$$W = 1.31 - 0.19 \times R_{Gen}^2 + 0.003 \times \left(R_{Gen}^2\right)^2. \tag{4.1}$$

Here $R_{Gen}$ is the *generated* radius of the $K_L^0$ at C6(see Chapter 2). This function also helped the match of $K_L^0$ transverse momentum between data and MC because the direction of $K_L^0$ momentum is the direction connecting the $K_L^0$ at C6 and the target with a smearing to account for the finite size of the target.

Please refer to [27] for more details on the tuning process. Here we will just show the overlay plots of different kinematic variables of our $K_L^0$ MC.

The momentum was generated from the function of:

$$\frac{dN}{dp} = N_0 exp(-\frac{(p-\mu)^2}{2\sigma^2}), \sigma = \sigma_0(1-(A+S\times p)(p-\mu)), \tag{4.2}$$

where $N_0$ is a normalization factor, $\mu = 1.79\ GeV/c$ is the mean of the distribution, $\sigma_0 = 1.29$ $GeV/c$ is the dispersion, $A = -0.33\ (GeV/c)^{-1}$ is the asymmetric offset, and $S = 0.03$ $(GeV/c)^{-2}$ is the asymmetric slope. The data and MC overlay is shown in Figure 4.1

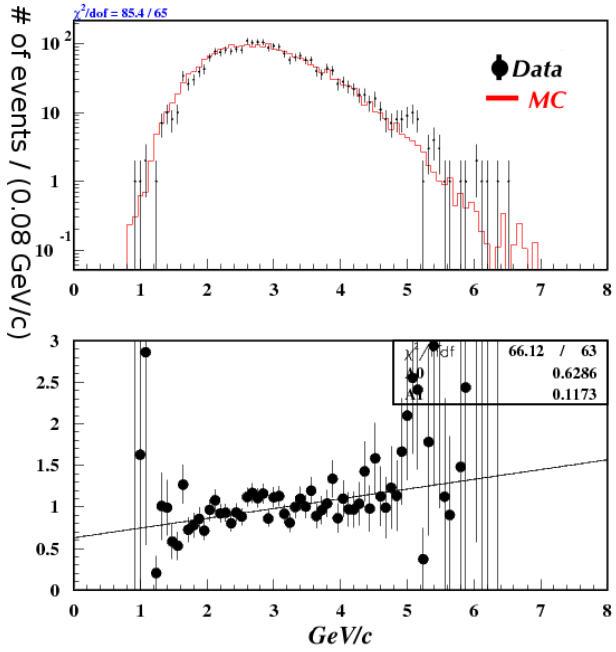


Figure 4.1: The reconstructed momentum distribution overlay of $K_L^0$ for four cluster($K_L^0 \to \pi^0\pi^0$) data and MC. The top plot shows data and MC together. And they are normalized by the total number of events. The bottom plot shows the bin-by-bin ratio of data and MC. The fit curve is a linear function. Errors on the top plot are counting errors($\sqrt{N}$). The $\chi^2/d.o.f.$ variable in the upper left-hand corner is a measure of bin-by-bin discrepancies. Unless noted, this setup is true for all the overlay plots in this thesis.

The Z vertex distribution in Figure 4.2 shows how well we do on the geometrical acceptance. The decay volume starts at 275cm, however the detector immediately before it(CC02) has a hole with a radius of 6cm. $K_L^0$'s decaying at or before CC02 have a chance to get accepted in reconstruction. The probability for that to happen is more suppressed as the

decay vertex is further away from the fiducial region. The suppression beyond 500cm is due to two facts: 1)photons will more likely fuse together as $K_L^0$ decay vertex is closer to CsI, 2)photons will more likely hit the center of calorimeter which is a hole surrounding by a veto detector(CC03) as $K_L^0$ decay vertex is closer to CsI.

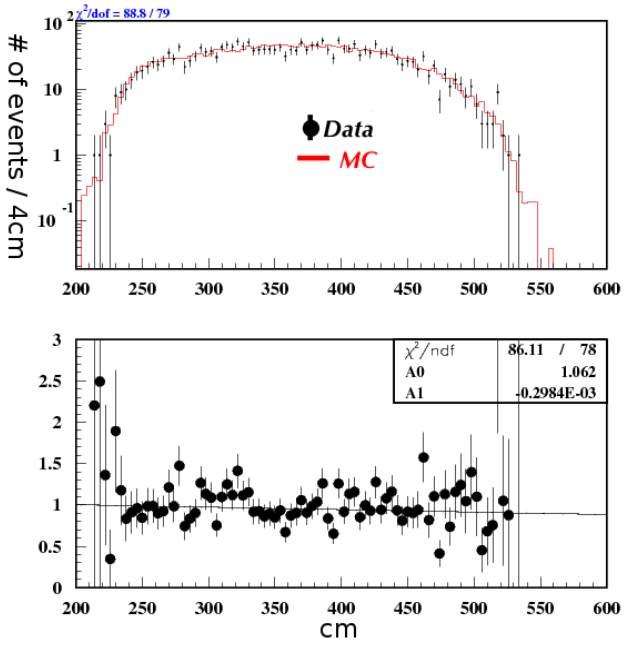


Figure 4.2: The reconstructed z vertex distribution overlay of $K_L^0$ for four cluster($K_L^0 \to \pi^0\pi^0$) data and MC. The z axis is defined as in Figure 2.3. The accepted decay region is from 340cm to 500cm.

The mass distribution in Figure 4.3 shows that the CsI energy resolution is the same in data and MC.

We show the contribution of $K_L^0 \to 3\pi^0$ and $K_L^0 \to \pi^0\pi^0$ for the four cluster invariant mass in Figure 4.4. $K_L^0 \to 3\pi^0$ dominates on the low mass tail. Its contribution to the $K_L^0$ mass peak is negligible.

The mass peak in the four cluster plot is squeezed by the sideband. To give a better look at the width of the peak, we show the six cluster comparison plot in Figure 4.5.

We generated $K_L^0$ at different radius at the end of the collimator according to:

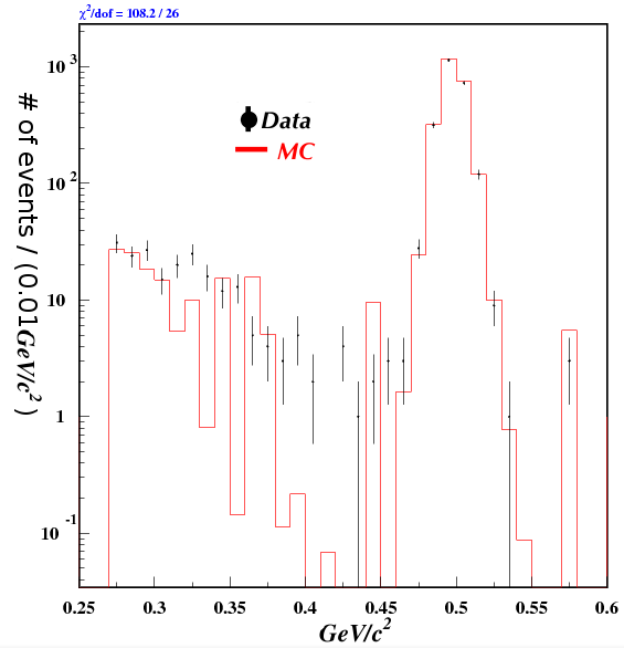


Figure 4.3: The reconstructed mass distribution overlay of $K_L^0$ for four cluster($K_L^0 \to \pi^0\pi^0$) data and MC. Note that in the sideband, $K_L^0 \to 3\pi^0$ is the dominant contribution. This plot is made by combining $K_L^0 \to \pi^0\pi^0$ and $K_L^0 \to 3\pi^0$ MC according to their branching ratios. The $K_L^0 \to 3\pi^0$ is heavily scaled due to limited statistics.

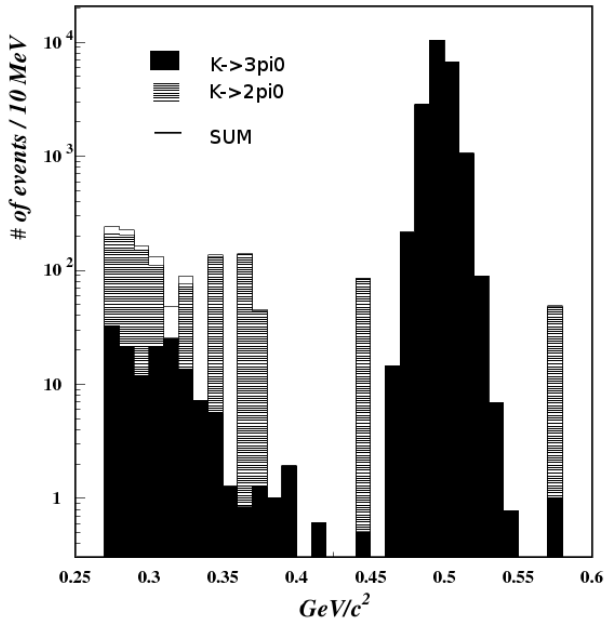


Figure 4.4: The reconstructed mass distribution of $K_L^0$ by sources for four cluster MC.

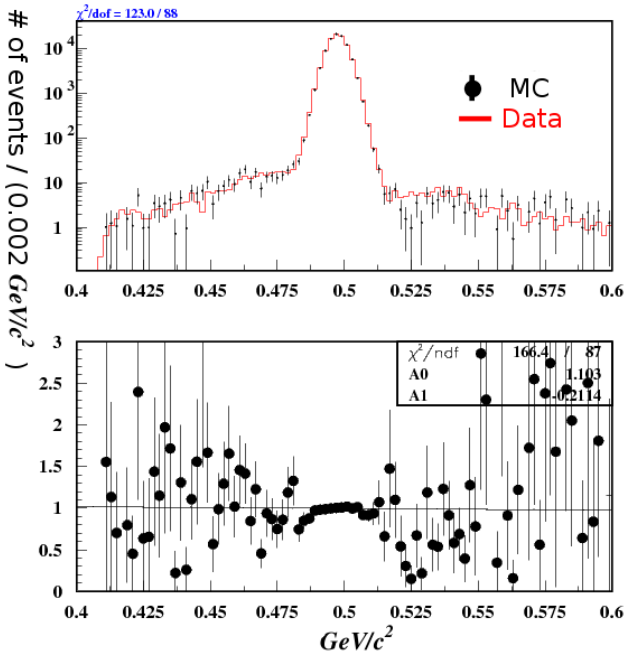


Figure 4.5: The reconstructed mass distribution overlay of $K_L^0$ for six cluster($K_L^0 \to 3\pi^0$) data and MC. $K_L^0 \to 3\pi^0$ itself fits the data in the whole mass region. And no other sources contributes to this plot.

$$\frac{dN}{dr} \approx \frac{N_0}{1 + exp((r - r_0)/s)}, \tag{4.3}$$

where $N_0$ is a normalization factor, $r_0 = 1.86cm$ is the falling edge, and $s = 0.21cm$ determines the slope of the falling edge. Once we have the position of the $K_L^0$, the polar angle of the beam is mostly determined by connecting the target and the $K_L^0$ position. The $K_L^0$ radial distributions match well between data and MC as shown in Figure 4.6.

The remaining discrepancy as indicated by a deviation from a straight line in the ratio plots of different variables was included in our systematic error as we calculate the same flux by varying the cuts.

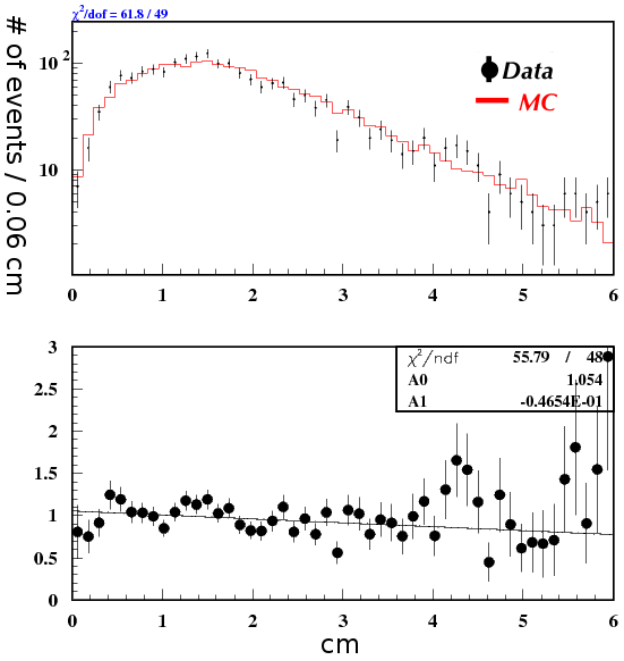


Figure 4.6: The reconstructed $K_L^0$ radius from beam axis at the end of collimators. This is a distribution overlay for four cluster($K_L^0 \to \pi^0\pi^0$) data and MC.

## 4.2 Detector Response

We simulated the detector response to different particles(mainly photons) using GEANT3 [35]. The secondary particles were traced to a cut off energy. The cut off energy was set as 50 keV for electrons, positrons and photons, and 100 keV for other particles. The energy response of each detector channel was taken as the sum energy in each module.

There were three exceptions to this: MB, CV and CsI. Since the first two detectors are too large. We have to take the light propagation and attenuation into account. For the main calorimeter - CsI, we also accounted for its energy resolution by applying smearing after the GEANT simulation. The details of these are described below.

**MB**

For MB, the light transmitted in the fibers can be think of as two component. These two component are attenuated differently along the fibers. But both can be described as

an exponential decay since the reflection behavior inside the scintillator is roughly uniform. This is so because its shape is uniform along the z-axis and the scintillator is long in the z direction.

To measure the attenuation function here, we can't just use a radioactive source. It's too weak to penetrate the module. We used cosmic ray to do this before the installation. We placed small plastic counters on both sides of the module and use the coincidence of them to determine the hit position in MB. We measured the parameters as [36]:

**CV**

The PMT response to the energy deposited in CV depends on the location of the hit. The weird shape of CV(see Figure 2.6) and the reflections in it make the dependence quite complicated. It's not even a monotonous function. The part close to the photo-multiplier tube(PMT) is in a uniform shape, and the light yield is determined by absorption in the scintillator itself while propagating. So the light yield decays in this region. The part far away from the PMT is shaped like the letter 'V'. Because all scintillators are wrapped with aluminum coated films to contain the light within the module itself, the odd shape at the far end enhances the light yield by this reflection. We measured the light attenuation function by radioactive source as in Figure 4.7. It was approximated by piece-wise linear functions. This was implemented in MC to model CV energy response correctly.

**CsI**

For CsI, we add smearing in addition to the GEANT 3 full shower simulation. This is for the consideration of photo-electron statistics, impurity and other things not included in GEANT 3. The criteria of the smearing is whether it reproduces the mass peak width of data. This is critical because the smearing affects the width of CC02 events as we will discuss in Chapter 5. For the veto detector, this treatment is not necessary and we package the result into the systematic error.

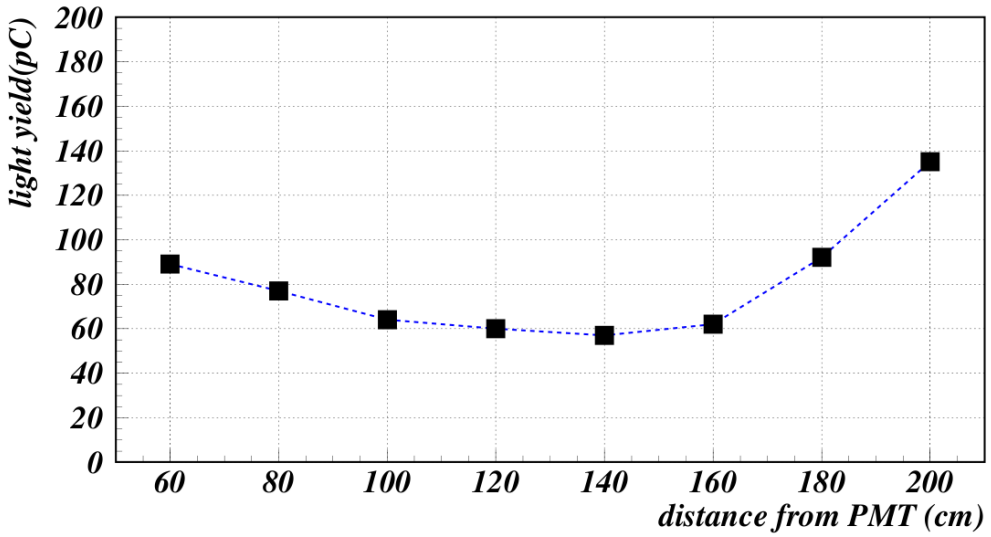


Figure 4.7: The light attenuation function of CV

## 4.3 Accidental Activity

Our MCs are targeted toward specific processes, and only one process is simulated in one set of MC. In our data, each event is also exposed to the ambient activity caused by all the other processes (not just other $K_L^0$ processes). We need to record the ambient activity - accidental data, and overlay that activity on top of the simulated events.

The accidental data was triggered by a target monitor, which is a plastic scintillator detector. Once we saw activity in the target, we took a snapshot of the entire detector. This trigger was heavily prescaled to have the rate to a manageable level.

The accidental data was overlayed to all the MC. For a specific MC event, we added the detector energy of a accidental event to the corresponding detector energy of MC. We took the earlier hit time as the new hit time in MC.

The accidental overlay affects the acceptance. It causes additional veto loss and also modifies the clustering in CsI.

## 4.4 Flux from Three Normalization Modes

The $K_L^0$ flux is calculated as shown in Table 4.1:

| Mode | number of events in data | acceptance | flux |
|---|---|---|---|
| $K_L^0 \to 3\pi^0$ | 48229 | $7.46 \times 10^{-5}$ | $3.30 \times 10^9$ |
| $K_L^0 \to \pi^0\pi^0$ | 1072 | $3.54 \times 10^{-4}$ | $3.48 \times 10^9$ |
| $K_L^0 \to \gamma\gamma$ | 14278 | $7.12 \times 10^{-3}$ | $3.66 \times 10^9$ |

Table 4.1: $K_L^0$ flux calculated independently from 3 normalization modes

We adopted the flux calculated from the $K_L^0 \to \pi^0\pi^0$ decay as our flux. Photons from the $K_L^0 \to \pi^0\pi^0$ have a similar energy range as photons from $K_L^0 \to \pi^0\nu\bar{\nu}$. This helps to reduce the systematic error when we use the flux together with the $K_L^0 \to \pi^0\nu\bar{\nu}$ acceptance.

A statistical uncertainty of 3% is determined by the number of $K_L^0 \to \pi^0\pi^0$ events accepted in data. We vary the cut condition on each cut by taking them out one by one. The response from data and MC is not exactly the same. This difference is used to calculate the uncertainty on the flux and acceptance. The detail of this process is described in [27]. We find the systematic uncertainty on the flux to be 6.3%. Overall we have a flux of:

$$(3.48 \pm 0.11_{stat} \pm 0.22_{sys}) \times 10^9. \tag{4.4}$$

These three modes is quite clean with our cuts. The contamination from halo neutron interaction and other $K_L^0$ decays is negligible.

## 4.5 A Detour

There was one detector material error we found in the previous versions of MC during the RunIII analysis. Its discovery started when we looked at the z vertex distribution of reconstructed $K_L^0$ in the neutral modes in Figure 4.8

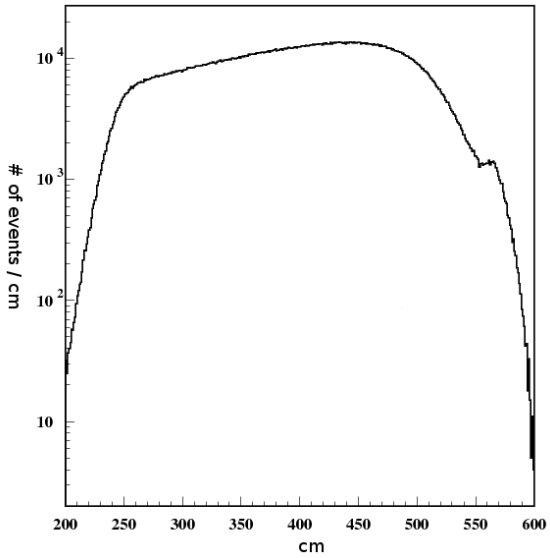


Figure 4.8: The reconstructed z vertex distribution of $K_L^0 \to \pi^0\pi^0$ MC before fixing the material error. The dip around z=555cm is right before the lead plate.

There was a clear dip in the MC z vertex distribution. We tried to look at the MC true decay point of $K_L^0$'s, but we saw nothing unusual.

The cause became clear when we looked at the x-y position scatter plot of photons at the lead plate for different z ranges in Figure 4.9. For $K_L^0$'s which decay before CV, there was a clear dent in the scatter plot. The dent mapped exactly to where a lead plate was. When we checked back on the original detector construction documents, we did find that there is a plate to support CV. But it's made of aluminum instead of lead.

In the data, about 90% of photons hitting the aluminum plate pass through. In the old MC, only 10% get through without interacting since the plate was wrongly implemented as lead. This destroyed many $K_L^0$ reconstructions when $K_L^0$'s decayed just in front of the plate and makes the dip in the z distribution. We corrected this material error and this problem disappeared.

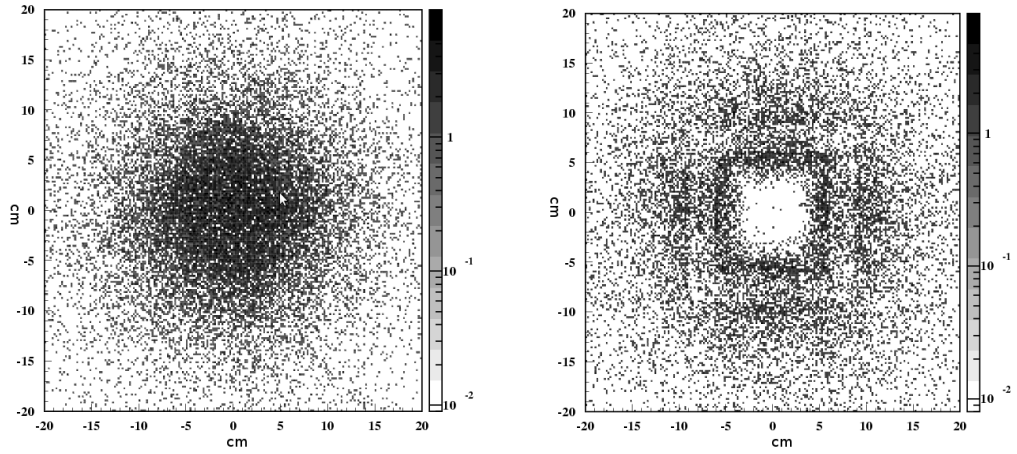


Figure 4.9: x-y position of photons at the lead plate. Beam axis is at the center. This plot is for $K_L^0 \to \pi^0\pi^0$ MC. The photon x-y position is get by using MC generation information of photon momentum and the $K_L^0$ decay point. A photon trajectory was extended to the lead plate(z = 566.485 cm) from the decay point in each event to calculate it. The left figure shows the $K_L^0$'s decaying behind the lead plate. And the right one is for events with z between 550cm and 552cm. A square dent defined by $|x| < 8.85cm, |y| < 8.85cm, |x| or |y| > 6.15cm$ is on the right figure, but not on the left one. The empty region at the center on the right figure is due to the pure geometrical acceptance of the calorimeter, which has a hole to let the beam go through. This empty region does not appear on the left figure because the trajectory of photons here were extended backward.

# CHAPTER 5

# BACKGROUNDS AND EVENT SELECTION

The background estimation was where most of the analysis work went. There are two background sources: 1) the interaction of halo neutron in the detector system, 2) $K_L^0$ decay processes other than $K_L^0 \to \pi^0\nu\bar{\nu}$. The former one is more tricky since the knowledge about what happens when the interaction of neutrons with energy in the range of a few GeV or less is limited. This is discussed in the first section. The last section of this chapter describes the $K_L^0$ related background. The $K_L^0$ related background is easier to estimate since it is determined mostly by electromagnetic shower. We also discuss a non-$K_L^0$ negligible background source - backward $\pi^0$'s from the vacuum vessel.

## 5.1 Halo Neutron Simulation and Background Estimation

In the RunII analysis the neutron background was treated with a combination of data driven analysis and multiple MCs [27][37]. The MC itself also had problem in producing the relative ratio of counts of $\pi^0$'s produced at CV and CC02. In various places, the simulation of previous analysis was also at a smaller statistics comparing with data. And the orthogonality of cuts had to be relied on for a bifurcation analysis to estimate the background.

A Monte Carlo using the Fluka model [38][39] was developed in RunIII analysis. This Monte Carlo simulated the neutron interaction as a whole. The CPU time was also reduced by early veto and recycling of secondary particles. The procedures, validation and result of this simulation is shown in this section.

### *5.1.1 Aluminum-target Run as a Check of the Physics Model*

The aluminum(Al)-target run was a special run we took to calibrate the main calorimeter originally. A 6 mm Al plate was placed in the beam after CC02. The trigger condition was the same as the physics trigger. Since there were about 60 times more neutrons than $K_L^0$'s in the beam [26], the events in this special run were mostly from neutron interactions. The Al-target run was an perfect independent check of the neutron interaction model.

In this special run we took the events with two clusters, and calculated the invariant mass of the two clusters assuming the vertex at the Al plate. The mass spectrum overlay between Al-target run data and MC is shown in Figure 5.1. We can clearly see two peaks, which correspond to $\pi^0$'s and $\eta$'s produced by neutrons(note: in this chapter we define $\eta$ as $\eta$ particle, not $\eta$ as one of the CKM matrix parameters in the Wolfenstein parametrization). The important thing is to check the relative height of the two peaks, because $\eta$-related background will be shown to be the dominant background.

The simulation was divided into two stage. In the first step, we simulated the neutron interactions at the aluminum target using the Fluka package. The daughter particles in each event were collected. The daughter particles were then passed to our Geant3 simulation. We set up our simulation in this way to use the existing software infrastructure.

The simulation and data matched well. We can use the neutron interaction models in Fluka including the production cross sections of $\pi^0$'s and $\eta$'s. The remaining discrepancy has been quantified to be 15% of systematic error on the background estimation.

In the middle and low mass region, the events are mainly one photon and one neutron. These events will be suppressed more than $\eta$ and $\pi^0$ events when we apply the photon quality cuts.

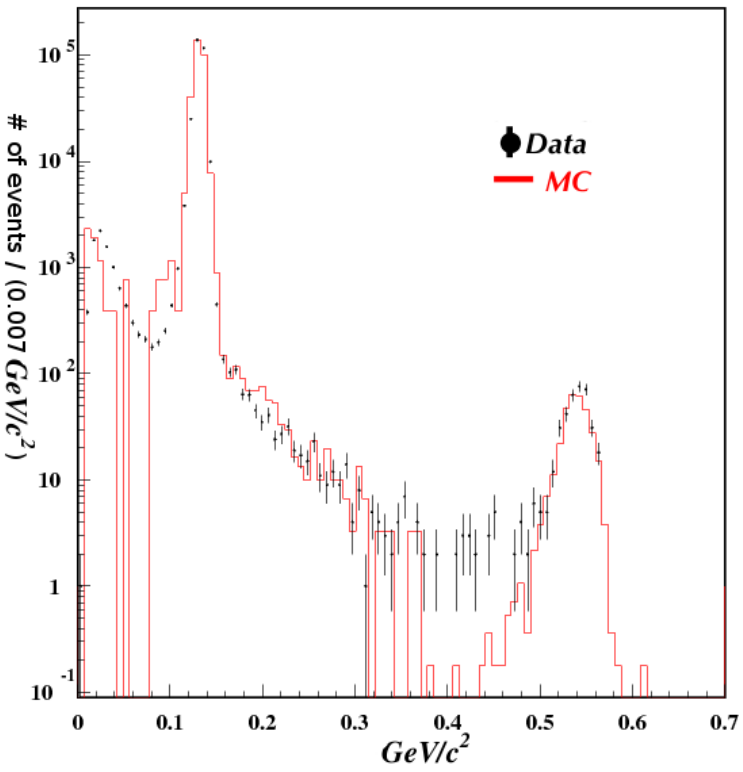


Figure 5.1: The reconstructed invariant mass spectrum of two cluster events in the aluminum target run with fixed vertex at the Al target. In addition to veto cuts, acoplanarity angle cut had been applied to get rid of $K_L^0 \to \gamma\gamma$ contribution. Note that different regions were produced in different second stage MC to speed up. The $\pi^0$ peak and low mass tail region are choppy due to limited statistics.

### *5.1.2 Halo Neutron Simulation*

Even with a great halo suppression, halo neutron interactions with detectors are still the dominant sources of background. The interactions mainly happen at the detectors like CC02 and CV, which are close to the beam. The low mass tail events produced at CC02 can come into the signal box. The high mass tail events produced at CV can come into the signal box. Neutrons also interact with the detectors and support structures that are close to the beam and behind CsI. But this contributes negligibly small background.

Like what we did for the core neutron simulation in the Al-target run, we also did the halo neutron simulation in two steps: 1) neutron interactions in Fluka, 2) photon showering in CsI by Geant3 based simulation. Unlike in Al-target run, the Al plate did not register energy, here the interacting materials were real detector materials. The energy registered in the detectors was used for veto. This reduced the number of events passed down to the second stage. The veto at the first stage together with recycling in the second stage improved the speed of simulation by a factor of 10.

Figure 5.2 shows the $\pi^0$ z vertex distribution overlay between physics run data and halo neutron MC in $K_L^0 \to \pi^0\nu\bar{\nu}$ reconstruction. Interactions with a single $\pi^0$ produced at CC02 and CV forms two peaks. The relative height of CV and CC02 $\pi^0$ peaks also confirms the neutron model.

The tails in the fiducial region is our biggest concern. We identified the physics mechanism behind these events. The dominant majority of these events were caused by $\eta$ particles produced by halo neutron at CV. $\eta$'s mass is $(547.853\pm0.024)MeV$. Since we found the vertex assuming the invariant mass of two clusters to be the $\pi^0$'s mass $(134.9766\pm0.0006)MeV$, the vertex was reconstructed into the fiducial region(z 340-500cm) rather than at the generation point at CV(z 560-610cm). The MC events are categorized by the secondary particles in Figure 5.3.

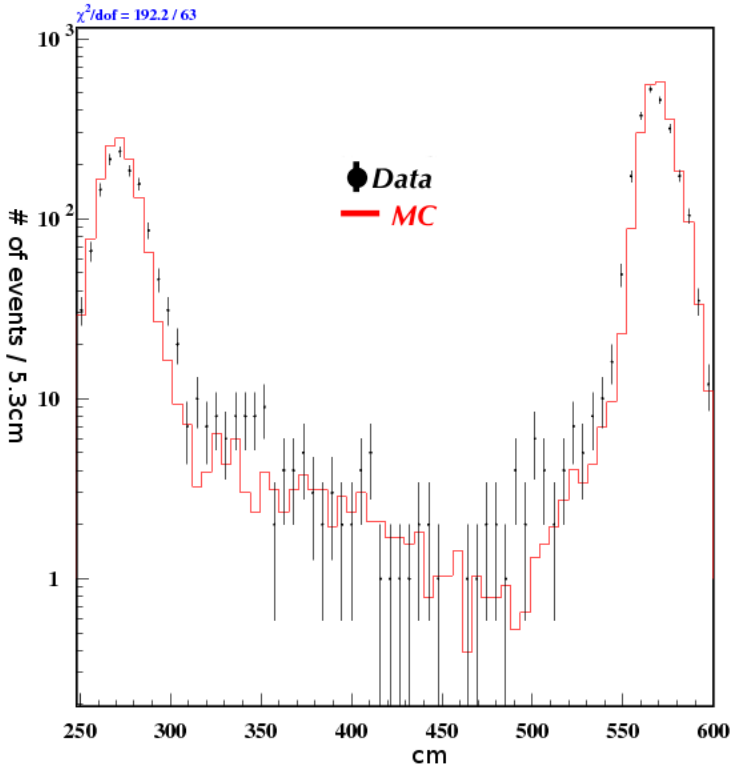


Figure 5.2: Reconstructed $\pi^0$ z vertex distribution overlay of data and halo neutron MC. Reconstructing $\pi^0$ from 2 cluster sample with vertex fixed on the beam axis is how we do the $K_L^0 \to \pi^0\nu\bar{\nu}$ reconstruction. Only veto cuts and photon quality cuts were applied. $K_L^0$ contribution was checked to be negligible.

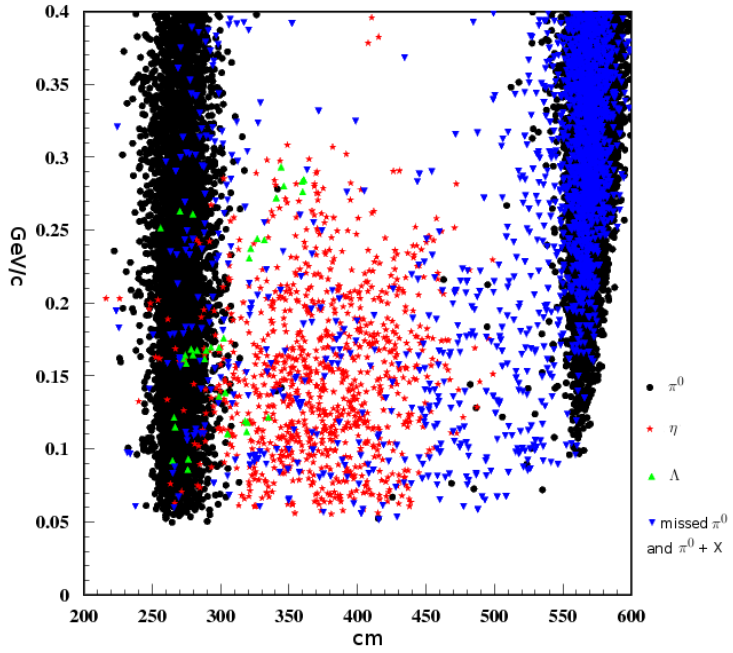


Figure 5.3: Physics mechanism for halo neutron interactions by secondary particles shown in scatter plot of transverse momentum and z vertex of reconstructed $\pi^0$. $\pi^0 + X$ means that there is other particles fused with the $\pi^0$'s photons in the CsI. The MC z vertex distribution in Figure 5.2 is the projection of this plot without events in the signal region.

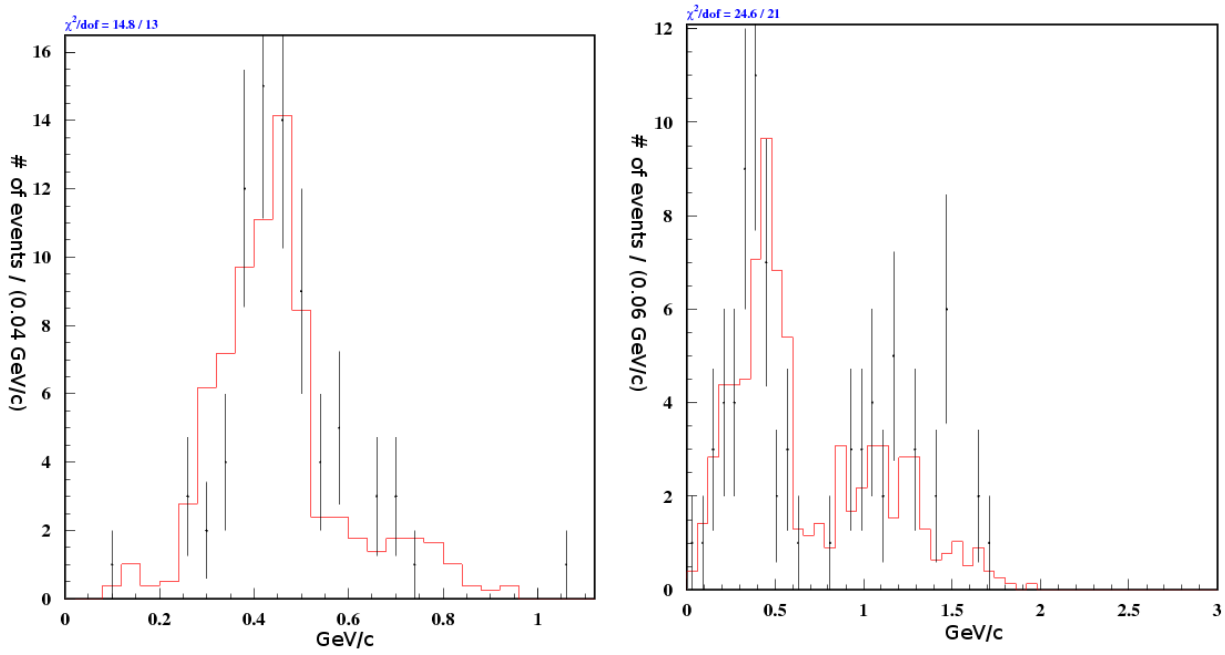


Figure 5.4: $\eta$ Momentum distribution of halo neutron CV $\eta$ events. This plot was made by reconstruction assuming $\eta$ mass. To keep our blind analysis rule, events were selected according to kinematic variables in $\pi^0$ reconstruction. We required $340cm < z(\pi^0) < 450cm$, and $P_T(\pi^0) < 0.12GeV/c$. The transverse momentum is shown at the top, and the longitudinal component is at the bottom.

Although not harmful in our experiment, we also found a new potential background: $\Lambda$ particle produced at CC02 by halo neutron interaction. About 35% of the time, it decays into a neutron and a $\pi^0$. Neutrons can escape the detector easily since our detector was mostly one interaction length of material. With the $\Lambda$ not being confined in the beam, the $\pi^0$ from its decay can have enough $P_T$ to fake a $K_L^0 \to \pi^0\nu\bar{\nu}$ event. However the life time of $\Lambda$ is about $2.6 * 10^{-10}$ second. It can not go into the fiducial region without decaying.

We also checked the momentum distribution of $\eta$'s in events under the signal box. This is shown in Figure 5.4.

To check if the momentum and z vertex correlation was correct, we also looked at transverse momentum and z vertex scatter plot. This is in Figure 5.5. The signal box is also drawn on this plot.

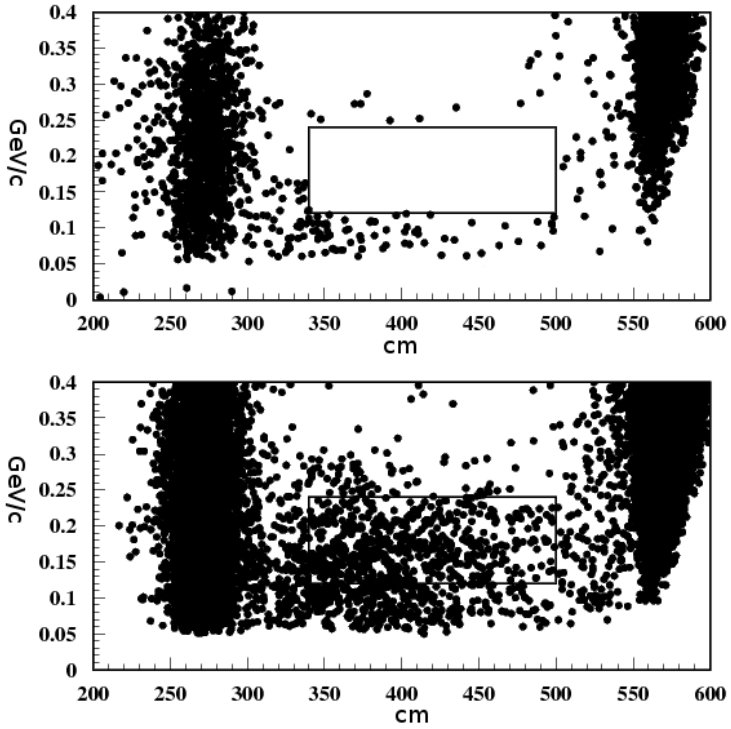


Figure 5.5: The $P_T$ vs. z plot of data and MC. Note that the cut condition is the same as in Figure 5.2. We have not applied the final cut yet.

Please note that to compare data with halo neutron MC, we applied the veto and other setup cuts to remove $K_L^0$ contributions. This also removed most of the hadronic shower events.

### *5.1.3 Event Selection Rules*

We applied many cuts to suppress the background. Two of them were particularly powerful in background rejection while had reasonably small acceptance loss. We will show the distribution of those cut variables in the $K_L^0 \to \pi^0\nu\bar{\nu}$ MC and the halo neutron MC. Note that to make these plots, we took out many cuts applied in the previous section.

**Fusion Cut**

There were usually tens of particles coming out as a neutron hit CC02 or CV. So most of the clusters in CsI from halo neutron interactions actually were caused hit of multiple particles. We trained a neural network algorithm to identify the multiple particle cluster (fused cluster) [40]. The distributions of the neural network output in the $K_L^0 \to \pi^0\nu\bar{\nu}$(signal) MC and the halo neutron (background) MC are shown in Figure 5.6.

**Angle Cut**

The most serious background comes from $\eta$ produced at CV by halo neutrons. One of the most effective cut against this background is the Angle Cut. The variable we cut on was the sum of the weighted difference of the reconstructed photon polar angle($\theta_{rec}$) and the polar angle($\theta_{clu}$) we found from the cluster shape [33] in two photons. The mathematical form of the definition is:

$$\sum_{\gamma} \Delta\theta\chi^2 = \sum_{\gamma} (\frac{\theta_{rec} - \theta_{clu}}{\sigma_{clu}})^2 \tag{5.1}$$

$\theta_{rec}$ is the photon polar angle calculated from the $\pi^0$ vertex and the photon position. $\theta_{clu}$ and $\sigma_{clu}$ are the polar angle and its uncertainty we got from a map established from a single photon Monte Carlo. At a given energy, the radial span of CsI defined in Equation 5.2 is

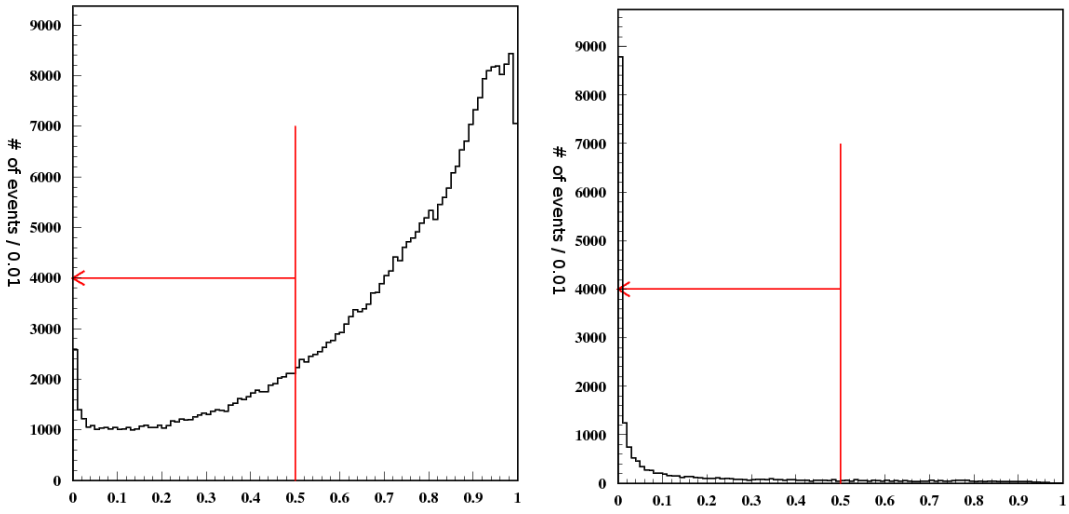


Figure 5.6: The fusion neural network output distribution of signal and halo neutron background. For all the cut variable distribution plots in this subsection including this one, the signal is on the left and the background is on the right. The red line with arrow shows the region which was rejected by the cut on the variable.

closely correlated with the photon polar angle. We built the map based on this. The typical value of $\sigma_{clu}$ is 9 degree.

$$RadialSpan = \sqrt{\frac{\sum_{crystals} e_i((r_i - r_0)P_l(\cos\alpha))^2}{\sum_{crystals} e_i}} \tag{5.2}$$

where $r_0$ is the position of the center of energy for the cluster. And $r_i$ and $e_i$ are the position and energy of the $i^{th}$ crystal in the cluster respectively. The angle $\alpha$ is the angle between the vector of $r_0$ and $r_i - r_0$.

The distributions of the cut variable $\sum_\gamma \Delta\theta\chi^2$ of signal and background are shown in Figure 5.7. $\sum_\gamma \Delta\theta\chi^2$ peaks around zero and has a narrow distribution while it peaks around 1.5 in the halo neutron $\eta$ background and has a wide spread to the higher values.

**Specifics of Other Cuts**

For all the cuts including the fusion cut and the angle cut, we categorized them into veto cuts and kinematic cuts. They are listed the following two tables for reference.

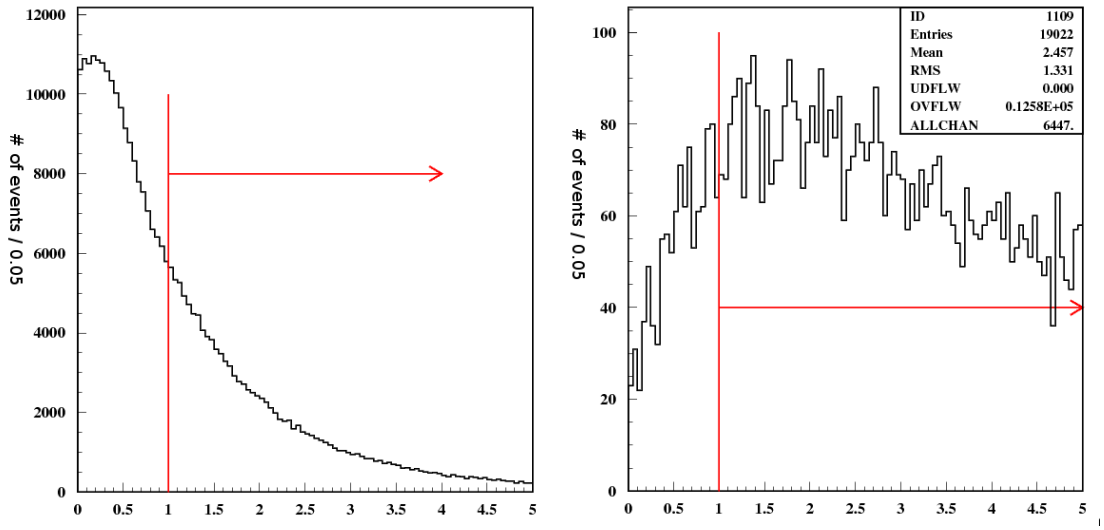


Figure 5.7: $\sum_\gamma \Delta\theta\chi^2$ distribution on signal and background. Note that there are lots of overflow events in background histogram. The background rejection power of this cut is about 95%.

Veto cuts are crucial for both halo neutron background and $K_L^0$ background. The specifics of these cuts are listed in Table 5.1.

The cuts in Table 5.2 select events based on the momentum, position and shape of the clusters. Some ensure a well reconstructed photon from CsI. Some reject background with the relation of the two photons and the reconstructed $\pi^0$'s. Some cuts are self-evident. Others are defined in the text or in the table. We explain the definition of two cuts below because the definition is too long to fit in the table.

**Minimum $K_L^0$ Momentum Cut**

The minimum possible $K_L^0$ momentum in the $K_L^0 \to \pi^0\nu\bar{\nu}$ kinematic constraints is calculated by assuming the invariant mass of the $\nu\bar{\nu}$ system is zero. With that constraint and the assumption the $P_T$ of the whole systems is balanced, we can solve for the four momentum

of the parent $K_L^0$.

$$\begin{aligned} M_{\nu\bar{\nu}} &\equiv 0 \\ A &= E_{\pi^0}^2 - P_{\pi^0,Z}^2 \\ B &= 0.5 \times (M_K^2 - M_{\pi^0}^2) - P_{\pi^0,T}^2 \\ D &= (B \times P_{\pi^0,Z})^2 - A \times (E_{\pi^0}^2 \times (P_{\pi^0,T}^2 + M_{\nu\bar{\nu}}^2) - B^2) \\ P_{miss} &= (B \times P_{\pi^0,Z} - \sqrt{D})/A \\ P_K &= P_{miss} + P_{\pi^0,Z} \end{aligned} \tag{5.3}$$

If the reconstructed $P_K$ is greater than 2 GeV/c, the event is rejected.

**$\pi^0$ Projection Cut**

When we looked at the scatter plot of momentum direction($P_T/P_z$) and z vertex of reconstructed $\pi^0$'s, we found that a cut shown in Figure 5.8 improving the signal to noise ratio. We call this the $\pi^0$ projection cut because the z and $p_T/P_z$ determines the length of the projection of the $\pi^0$ momentum vector on CsI. Most of the background events in the signal box are produced by interactions at CV. Even with z mis-reconstructed for $\eta$ events they have a smaller $\pi^0$ momentum projection length on CsI. The limit set by the lower lines in Figure 5.8 is particularly effective.

### *5.1.4 Background Estimation*

With all the cuts applied, we show the transverse momentum versus z vertex scatter plot of data and MC in Figure 5.9. We saw two events inside the signal box for MC. And they were all $\eta$ events.

The normalization factor of MC to data is $6.5 \pm 0.8$. We have two events in the signal box for halo neutron MC. So the background prediction is: $0.31 \pm 0.22_{stat} \pm 0.10_{sys}$.

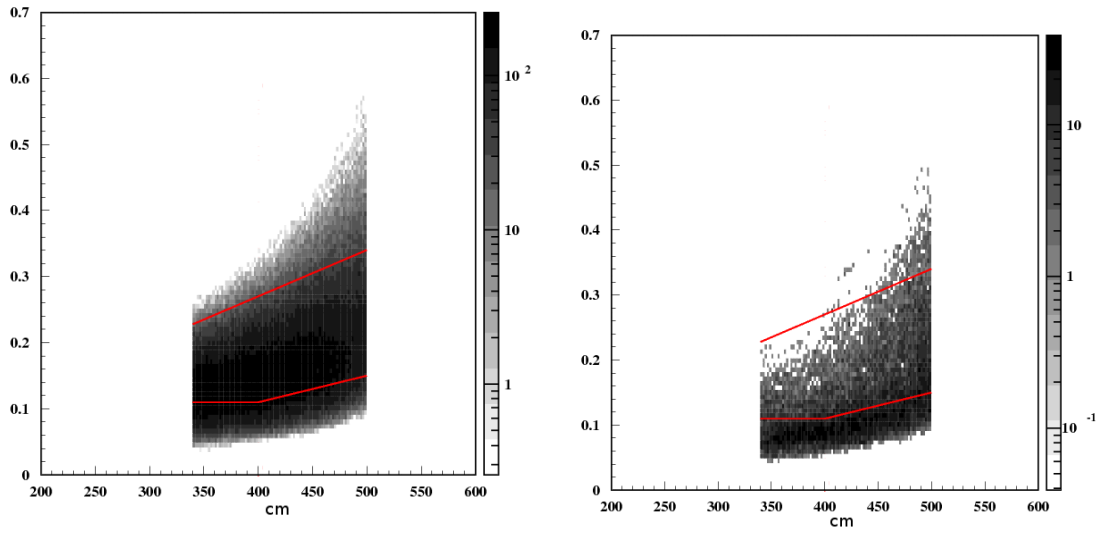


Figure 5.8: $\pi^0$ projection cut on signal and halo neutron background. Because we only show events in the signal box, the vertex distribution is restricted to be between 340cm and 500cm. The events between the three red lines are kept.

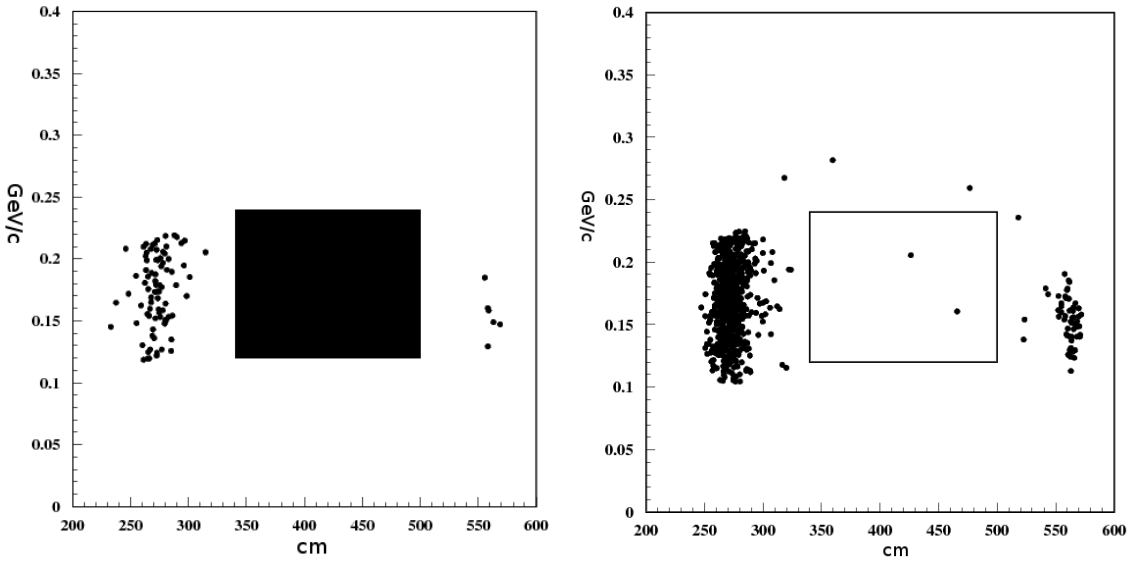


Figure 5.9: $P_T$ vs. z scatter plot of the data and halo neutron MC with final cuts. Note that the signal region in data is covered. The normalization factor of MC to data is $6.5 \pm 0.8$.

The systematic error comes from the uncertainty on the $\pi^0$ / $\eta$ ratio, normalization at different cut level and remaining mismatch.

## 5.2 Other Negligible Backgrounds

We will discuss other potential backgrounds in this section. They are all small. Three out of four of them are $K_L^0$ related. $K_L^0$'s other decay can pose as a background to $K_L^0 \to \pi^0\nu\bar{\nu}$ because extra particle can go undetected or fused with other particles in CsI. The relevant modes are $K_L^0 \to \pi^0\pi^0$, charged mode decays, and $K_L^0 \to \gamma\gamma$. The other one is caused by backward $\pi^0$'s from the materials behind CsI.

### *5.2.1* $K_L^0 \to \pi^0\pi^0$

This mode is the most serious background candidate among all $K_L^0$ decay related ones. The extra two photon can either miss the veto system or get fused together with other photons.

The $K_L^0 \to \pi^0\pi^0$ background can be estimated from the $K_L^0$ Monte Carlo simulation. The biggest issue here is to verify that MC estimates the photon veto inefficiency and fusion probability right.

This can be done through a similar process:$K_L^0 \to 3\pi^0$ faking $K_L^0 \to \pi^0\pi^0$ signal with a low mass. The extra two photon get lost through the same mechanism. Unlike $K_L^0 \to \pi^0\pi^0$ faking $K_L^0 \to \pi^0\nu\bar{\nu}$, the vertex of the $K_L^0$ decay is found by the two $\pi^0$. So we are actually looking at the low mass tail generally. The plots is in Figure 4.3.

Figure 5.10 shows that what happens if we don't have a veto system. There is a event cluster around z=250cm. This is right before CC02. CC02 blocks some photons of the 4 photons from $K_L^0 \to \pi^0\pi^0$. This makes events more likely to be a two-cluster events. So there are more events in this z 250cm region.

With all cuts applied, we saw no events for a $K_L^0 \to \pi^0\pi^0$ MC with 10 times more

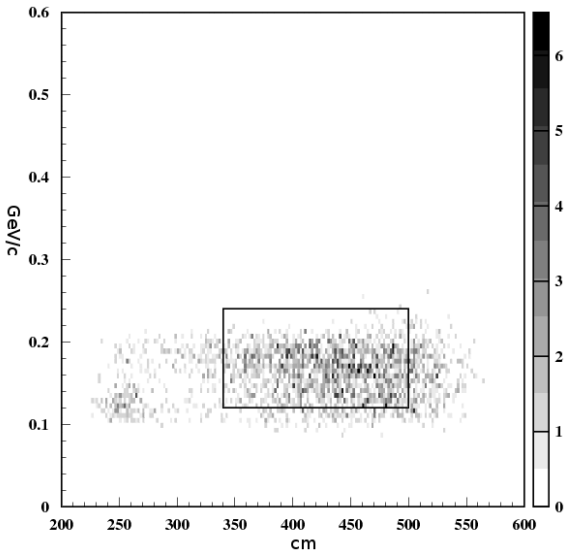


Figure 5.10: The $P_T$ vs. z plot of $K_L^0 \to \pi^0\pi^0$ MC by $K_L^0 \to \pi^0\nu\bar{\nu}$ reconstruction. Only the non-veto cuts applied .

$K_L^0 \to \pi^0\pi^0$ decay than data. We set the background estimation from $K_L^0 \to \pi^0\pi^0$ as $< 0.1$.

### *5.2.2 Backward $\pi^0$'s*

This potential background concerns backward going $\pi^0$ from halo neutron interaction at the vacuum vessel end-cap, which is about 2 meters behind CsI.

The simulation that we had was for interactions before CsI only. The interactions behind CsI could be a background if the $\pi^0$s produced by neutrons went backward toward CsI. We had no way of knowing whether the photons come from the fiducial region or behind CsI. We only checked the interactions behind CsI on the vacuum vessel end-cap since it was the only significant dead material behind CsI. It was also more important than other materials behind the CsI because its image was right in the middle fiducial region.

With just veto cuts, we were left with events in Figure 5.11. With all cuts applied, no events were left. This simulation corresponded to 50 times data statistics in terms of the number of halo neutron interactions. Thus this background was estimated to be $< 0.02$.

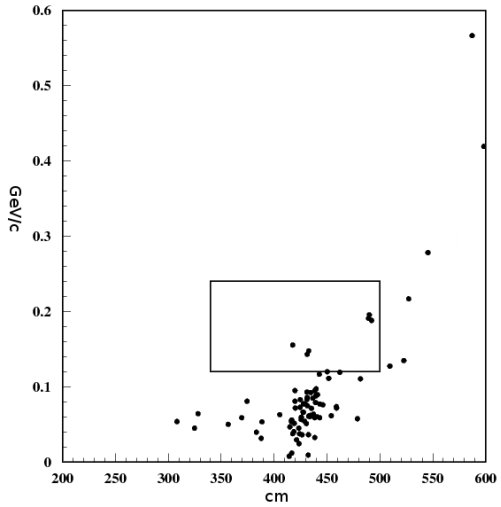


Figure 5.11: $P_T$ vs. z plot of halo neutron backward $\pi^0$ events from the vacuum vessel end-cap with only veto cuts. Events produced at larger radius was reconstructed with larger $P_T$ and z because we fixed the vertex on the beam axis.

### *5.2.3 $K_L^0$ Charged Mode Decay*

The charged mode decay constitutes about 80% of the $K_L^0$ decay branching ratio. It includes $K_L^0 \to \pi^{\pm} e^{\mp} \nu$, $K_L^0 \to \pi^{\pm} \mu^{\mp} \nu$ and $K_L^0 \to \pi^+ \pi^- \pi^0$. These decay modes are the reason that we must have the scintillator panels directly in front of CsI. Otherwise we won't know if the two clusters in CsI is caused by photons or charged particles from these decays.

Muons do not produce showers among CsI blocks. So the $K_L^0 \to \pi^{\pm} \mu^{\mp} \nu$ background contribution is smaller than the $K_L^0 \to \pi^{\pm} e^{\mp} \nu$ background. $K_L^0 \to \pi^+ \pi^- \pi^0$ decay has extra particles in the final state to fake a two-cluster event. The transverse momentum of the $\pi^0$ is also limited. The biggest background among the charged modes is from $K_L^0 \to \pi^{\pm} e^{\mp} \nu$. We focus on the $K_L^0 \to \pi^{\pm} e^{\mp} \nu$ decay in the following part.

To study this background, we made $K_L^0 \to \pi^{\pm} e^{\mp} \nu$ MC(relying on the general $kl$ MC) and applied all cuts except CV cut after reconstruction. These events are shown in Figure 5.12. As shown in Chapter 3,we can use a upper limit of $10^{-4}$ for the CV inefficiency.

Considering the CV suppression factor and normalization by $K_L^0$ flux, we estimated the

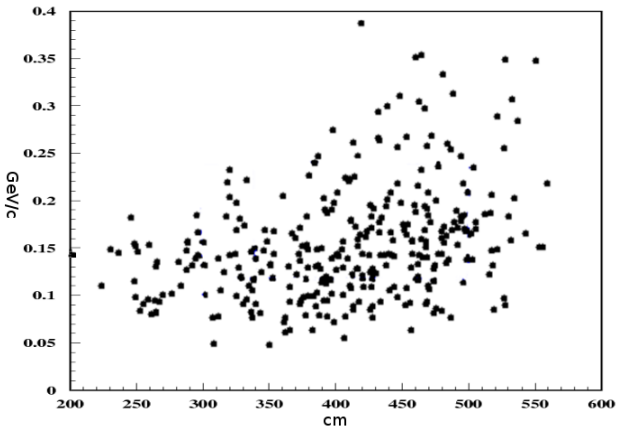


Figure 5.12: The $P_T$ vs. z plot of $K_L^0 \to \pi^{\pm} e^{\mp} \nu$ MC by $K_L^0 \to \pi^0 \nu\bar{\nu}$ reconstruction. All cuts applied except for the charged veto cuts.

background from $K_L^0 \to \pi^{\pm} e^{\mp} \nu$ to be $(3.9 \pm 0.6) \times 10^{-4}$.

### *5.2.4* $K_L^0 \to \gamma\gamma$

Two photons in this decay could naturally make the cluster part of the signal. But the $\pi^0$ reconstructed from the $K_L^0 \to \gamma\gamma$ event has low transverse momentum. And even in the low $P_T$ region, $K_L^0 \to \gamma\gamma$ is greatly suppressed by the acoplanarity angle cut, defined as:

$$\theta_{acop} = \pi - \arccos\left(\frac{u \cdot v}{|u||v|}\right), \tag{5.4}$$

where $u$ and $v$ are vectors pointing from the center of CsI array to the reconstructed cluster positions in the face-plane of the calorimeter. This is shown in Figure 5.13.

The distributions of $\theta_{acop}$ in $K_L^0 \to \gamma\gamma$ and $K_L^0 \to \pi^0 \nu\bar{\nu}$ are shown in Figure 5.14. A cut at 75 degree removes $K_L^0 \to \gamma\gamma$ background completely. The background from $K_L^0 \to \gamma\gamma$ is $< 10^{-5}$. Note that this cut was also used in analysis in addition to the cuts in Table 5.1 and 5.2.

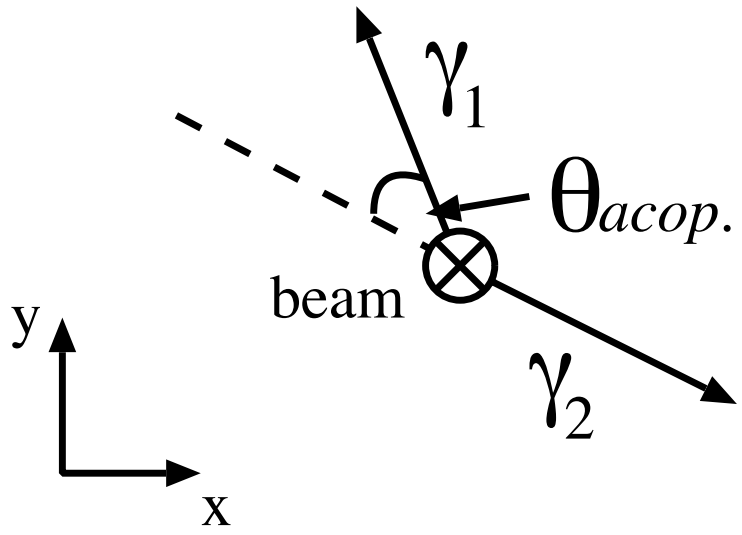


Figure 5.13: The acoplanarity angle as defined in Equation 5.4.

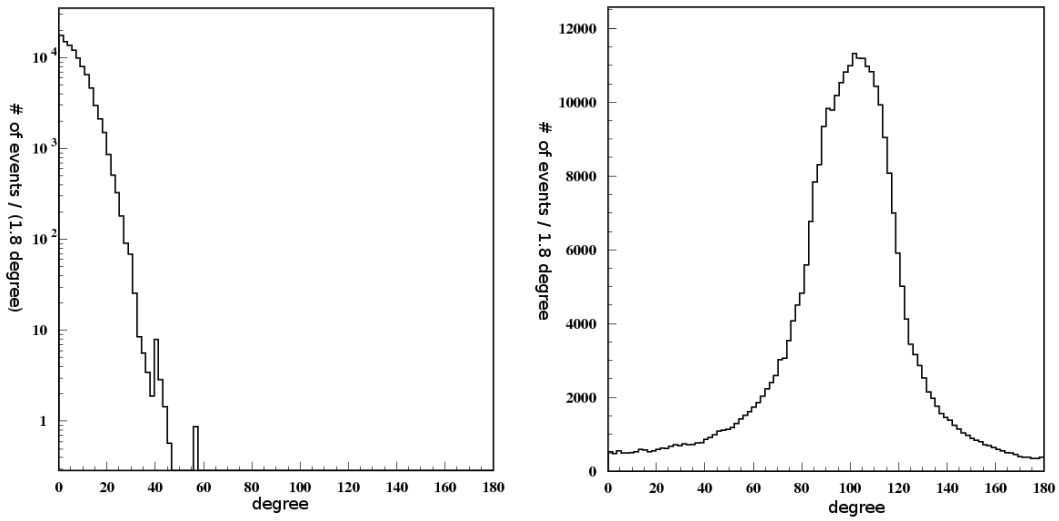


Figure 5.14: $\theta_{acop}$ in $K_L^0 \to \gamma\gamma$ and $K_L^0 \to \pi^0\nu\bar{\nu}$ MC, with $K_L^0 \to \gamma\gamma$ at the top and $K_L^0 \to \pi^0\nu\bar{\nu}$ at the bottom.

| Detector | Energy Cut | Comments |
|---|---|---|
| CC00 | 2 MeV | |
| Front Barrel | 1 MeV | Inner & Outer Sum. |
| CC02 | 1 MeV | |
| Barrel CV | 0.75 MeV | $\sqrt{Up \times Down}$ (w/TDC). |
| Inner Main Barrel | 1 MeV | $\sqrt{Up \times Down}$ (w/TDC). |
| Outer Main Barrel | 1 MeV | $\sqrt{Up \times Down}$ (w/TDC). |
| Outer CV | 0.3 MeV | |
| Inner CV | 0.7 MeV | |
| CC03 | 2 MeV | |
| CsI: S-Hit Close | 5 MeV | Crystal $d < 17$ cm from closest cluster. |
| CsI: S-Hit Intermediate | 5 - $(7/40)(d - 20)$ MeV | Crystal is $d$ cm from closest cluster. |
| CsI: S-Hit Far | 1.5 MeV | Crystal $d > 40$ cm from closest cluster. |
| Sandwich Counters | 2 MeV | |
| CC04 Charged Layer | 0.7 MeV | |
| CC04 Calorimeter Layer | 2 MeV | |
| CC05 Charged Layer | 0.7 MeV | |
| CC05 Calorimeter Layer | 3 MeV | |
| CC06 | 10 MeV | Cerenkov detector with MIP calibration |
| CC07 | 10 MeV | Cerenkov detector with MIP calibration |
| BHCV | 0.1 MeV | |
| BA Scintillator<br>BA Quartz | 30 MeV<br>0.5 MIPs | Sum over layers.<br>Max. layer.<br>(AND logic.) |

Table 5.1: The veto cuts.

| Cut | Values | Cut Variable Definition |
|---|---|---|
| Higher Energy $\gamma$ E-Min. | 250 MeV | |
| Lower Energy $\gamma$ E-Min. | 150 MeV | |
| $\gamma$ CsI Hit Position | $18 < r < 88$ cm | |
| $\gamma$ Hit Separation Min. | 30 cm | |
| $\gamma$ Hit timing $= T_H - T_L$ | $-3.4 < \Delta T < 2.89$ ns | |
| $\pi^0$ Energy Max. | 1.5 GeV | |
| $\gamma$ RMS Max. | 5.2 | $\sqrt{\frac{\sum_i e_i \times (r_i - r_0)^2}{\sum_i e_i}}$. $r_0$ is the cluster's center of energy position. $r_i$ and $e_i$ are the position and energy of its $i^{th}$ crystal. |
| $\sum_\gamma \Delta\theta\chi^2$ Max. | 1 | See Text |
| $\gamma$ Energy Ratio Min. | 0.92 | $\frac{e_1+e_2+e_3}{E_{dep}}$. $e_1, e_2$ and $e_3$ are the cluster's three largest crystal energies. $E_{dep}$ is the energy sum of all crystals. |
| Fusion Neural Network | 0.5 | See Text |
| TDI Max. | 2 | $\frac{1}{N}\sqrt{\sum_i (T_i - T_m)^2}$, $N$ is the number of crystals in the cluster. $T_i$ is the time of the $i^{th}$ crystal. $T_m = \frac{1}{N}\sum_i T_i$. |
| $\gamma$ Energy Balance Max. | 0.6 | $(E_H - E_L)/(E_H + E_L)$ |
| Crystal Size Min. | 5 | 1 MeV threshold |
| $\pi^0$-projection | | See Text. |
| Minimum $K_L^0$ Momentum | | See text. |
| $\pi^0$ Transverse Momentum | $0.12 GeV/c < P_T < 0.24 GeV/c$ | |
| $\pi^0$ z Vertex | $340cm < z < 500cm$ | This cut and the $P_T$ cut constitute the signal box selection. |

Table 5.2: Kinematic Cuts for $K_L^0 \to \pi^0\nu\bar{\nu}$ Events. The cut variables that are well defined in their names are not repeated.

# CHAPTER 6

# CONCLUSIONS

With the understanding of all possible backgrounds, we opened the covered box and made our final measurement on $K_L^0 \to \pi^0\nu\bar{\nu}$. In the first part of this chapter, we describe the acceptance and sensitivity. In the second part of this chapter, we show the final result. And in the last part, we discuss the future prospect.

## 6.1 Acceptance and Sensitivity

The single event sensitivity is defined as:

$$\text{S.E.S.}(K_L^0 \to \pi^0\nu\bar{\nu}) = \frac{1}{F \times A}, \tag{6.1}$$

where $F$ is the $K_L^0$ flux, calculated from the normalization modes in Chapter Chapter 4, and $A$ is the acceptance for $K_L^0 \to \pi^0\nu\bar{\nu}$.

The acceptance of $K_L^0 \to \pi^0\nu\bar{\nu}$ was computed through the use of the MC with the same MC as the normalization modes. Figure 6.1 shows the $K_L^0 \to \pi^0\nu\bar{\nu}$ events with the event selection rule established in Chapter 5. We had 44057.86 events in the signal box, and 4251098.0 Kl decay in the fiducial region(340cm-500cm). Note that the numbers are not integer because we weighted the events according to the $K_L^0$ radius at the end of collimators.

Adding the acceptance loss due to time-related cut, which was not well simulated [37], our acceptance is: $44057.86/4251098.0 \times 0.967^2 \times 0.974 \approx 0.94\%$

The systematic error on the acceptance comes from the same physics mechanism involving detector material, geometry, and shower modeling. Since we don't have $K_L^0 \to \pi^0\nu\bar{\nu}$ data to guide us on this, we use the value we obtained for the normalization mode($K_L^0 \to \pi^0\pi^0$, but other modes have a similar value):$6.3\% \times \textit{Acceptance}$:

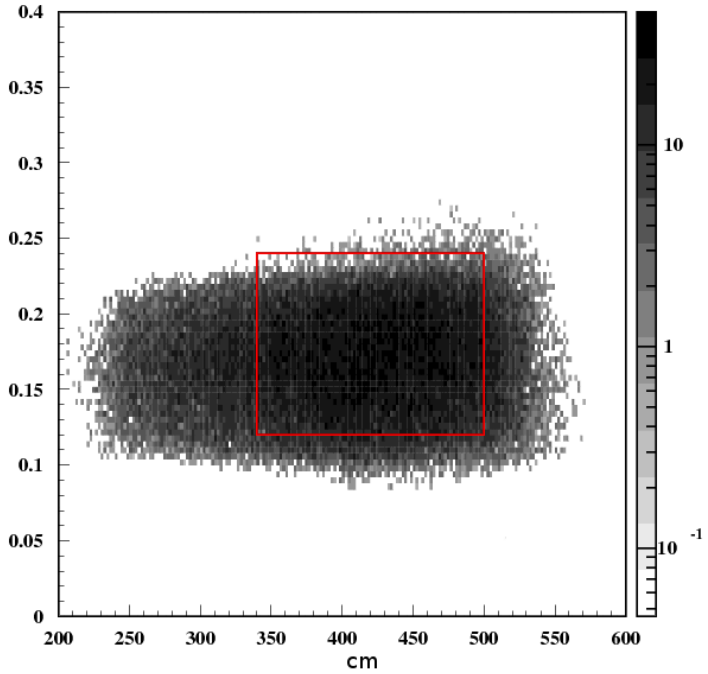


Figure 6.1: $P_T$ versus z plot of $K_L^0 \to \pi^0\nu\bar{\nu}$ MC with cuts specified in Table 5.1 and 5.2.

$$Acceptance(K_L^0 \to \pi^0\nu\bar{\nu}) = (0.94 \pm 0.06)\% \tag{6.2}$$

The accidental loss was included by the same accidental overlay in the normalization and background MC. Overall the accidental loss is about 17%. It mainly came from the veto on MB and CsI, about 7% each.

Combining the acceptance with the flux in Equation 4.4, we got a single event sensitivity of:

$$S.E.S. = (3.0 \pm 0.1_{stat} \pm 0.3_{sys}) * 10^{-8} \tag{6.3}$$

## 6.2 Final Results

We opened the covered box with all cuts imposed. And there was no event in the signal region. This is shown in Figure 6.2

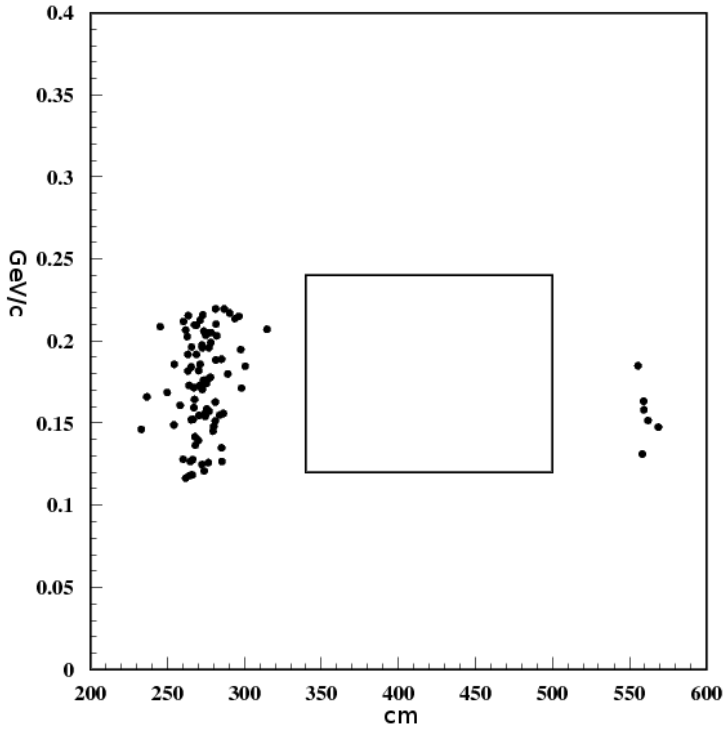


Figure 6.2: Data final $P_T$ vs. z plot with signal box opened.

Using a correction to the simple Poisson statistics to incorporate the uncertainty on the single event sensitivity, we set the upper limit on the branching ratio of $K_L^0 \to \pi^0\nu\bar{\nu}$ measured from RunIII data as [41]:

$$Br(K_L^0 \to \pi^0\nu\bar{\nu}) < 2.3 \times (1 + 2.3/2 \times (0.27/3.0)^2)3.0 \times 10^{-8} = 6.96 \times 10^{-8} \qquad (6.4)$$

at the 90% Confidence Level.

This is consistent with the Standard Model.

## 6.3 Future $K_L^0 \to \pi^0\nu\bar{\nu}$ Search

In summary, the largest background in E391 is due to the interactions of halo neutrons with CV and CC02 detector materials, especially CV. The background rejection power is also

limited by the size of the CsI block. The next experiment searching for $K_L^0 \to \pi^0\nu\bar{\nu}$ - E14 at Japan Proton Accelerator Research Complex(J-Parc) will improve upon these things. We have an optimized beam to reduce the halo neutron activity. A much finer segmented CsI will also be used. We also have an easy fix - moving CV and CC02 further away from the beam and the decay region. Based on what we learned in E391a and this analysis, E14 will reach two orders of magnitude beyond the Standard Model sensitivity.

# REFERENCES


[1] T. D. Lee and C. N. Yang. Question of Parity Conservation in Weak Interactions. *Physical Review*, 104(254), 1956.

[2] C. S. Wu et al. Experimental Test of Parity Conservation in Beta Decay. *Physical Review*, 105, 1957.

[3] J. H. Christenson, J. W. Cronin, V. L. Fitch, and R. Turlay. Evidence for the $2\pi$ decay of the $K_2^0$ meson. *Physical Review Letters*, 13(4), 1964.

[4] M. Kobayashi and T. Maskawa. $CP$ Violation in the Renormalizable Theory of Weak Interactions. *Progress of Theoretical Physics*, 49(2), 1973.

[5] Stephen Barr et al. Magnitude of the cosmological baryon asymmetry. *Physical Review D*, 20(10), 1979.

[6] A. Alvi-Harati et al. Measurements of Direct CP Violaiton, CPT Symmetry, and Other Parameters in the Neutral Kaon System. *Phys. Rev. D*, 67(012005), 2003.

[7] V. Prasad. *Measurements of the Direct CP-Violation and CPT-Invariance in the Neutral Kaon System*. PhD thesis, The University of Chicago, 2002.

[8] C. Amsler et al(Particle Data Group). *Physics Letters B*, 667:1, 2008.

[9] L. Wolfenstein. Parametrization of the Kobayashi-Maskawa Matrix. *Physical Review Letters*, 51(21), 1983.

[10] C. Jarlskog. Commutator of the Quark Mass Matrices in the Standard Electroweak Model and a Measure of Maximal $CP$ Nonconseration. *Physical Review Letters*, 55(10), 1985.

[11] J. Charles et al. *Eur. Phys. J. C*, 41:1–131, 2005.

[12] A. J. Buras et al. Waiting for precise measurements of $K^+ \to \pi^+\nu\bar{\nu}$ and $K_L^0 \to \pi^0\nu\bar{\nu}$. hep-ph/0405132, 2004.

[13] F. Mescia and C. Smith. Improved esitmates of rare $K$ decay matrix-elements from $K_{l3}$ decays. arXiv:0705.2025v1, 2007.

[14] T. Inami et al. Effects of Superheavy Quarks and Leptons in Low-Energy Weak Process $K_L^0 \to \mu\bar{\mu}$, $K^+ \to \pi^+\nu\bar{\nu}$ and $K^0 \leftrightarrow \bar{K^0}$. *Progress of Theoretical Physics*, 65(297), 1981.

[15] A.J. Buras et al. $K^+ \to \pi^+\nu\bar{\nu}$ and $K_L^0 \to \pi^0\nu\bar{\nu}$ Decays in the General MSSM. hep-ph/0408142, 2004.

[16] A. J. Buras et al. Anatomy of Prominent $B$ and $K$ Decays and Signatures of CP-Violating New Physics in the Electroweak Penguin Sector, 2004.

[17] A. J. Buras et al. $B \to \pi\pi$, New Physics in $B \to \pi K$, and Implications for Rare $K$ and $B$ Decays. *Physical Review Letters*, 92(10), 2004.

[18] Christoph Bobeth et al. Upper bounds on rare $K$ and $B$ decays from minimal flavour violation. *Nuclear Physics B*, 726:252–274, 2005.

[19] A. J. Buras et al. The Impact of Universal Extra Dimensions on the Unitarity Triangle and Rare $K$ and $B$ Decays. hep-ph/0212143, 2003.

[20] S. Rai Choudhury et al. $K_L^0 \to \pi^0\nu\bar{\nu}$ in Little Higgs Model. *hep=ph/0408125*, 2005.

[21] A. J. Buras et al. Non-Decoupling Effects of the Heavy $T$ in the $B_{d,s}^0 - \bar{B}_{d,s}^0$ Mixing and Rare $K$ and $B$ Decays. hep-ph/0501230, 2005.

[22] G. Graham et al. Search for the Decay $K_L^0 \to \pi^0\nu\bar{\nu}$. *Phys. Lett.*, B295:169–173, 1992.

[23] A. Alavi-Harati et al. Search for the decay $K_L^0 \to \pi^0\nu\bar{\nu}$ using $\pi^0 \to e^+e^-\gamma$. *Physical Review D*, 61, 2000.

[24] J. K. Ahn et al. New limit on the $K_L^0 \to \pi^0\nu\bar{\nu}$ decay rate. *Phys. Rev. D (RC)*, 74(051105(R)), 2006.

[25] J. K. Ahn et al. Search for the Decay $K_L^0 \to \pi^0\nu\bar{\nu}$. *Physical Review Letters*, 100(201802), 2008.

[26] H. Watanabe et al. Neutral beam line to study $K_L^0 \to \pi^0\nu\bar{\nu}$ decay at the KEK 12-GeV proton synchrotron. *Nuclear Instruments and Methods in Physics Research A*, 545:542–553, 2005.

[27] G. Perdue. *Search for the rare decay* $K_L^0 \to \pi^0\nu\bar{\nu}$. PhD thesis, The University of Chicago, 2008.

[28] K. Sakashita. *Search for the decay* $K_L^0 \to \pi^0\nu\bar{\nu}$. PhD thesis, Osaka University, 2006.

[29] CERN. GEANT 4.8.3.

[30] H. S. Lee. *Search for the Rare Decay* $K_L^0 \to \pi^0\nu\bar{\nu}$ *at E391a.* PhD thesis, Pusan National University, 2007.

[31] M. Doroshenko. Calibration of E391 detector. Internal Tech-Note, 2007.

[32] M. Doroshenko et al. Undoped CsI calorimeter for the $K_L^0 \to \pi^0\nu\bar{\nu}$ experiment at KEK-PS. *Nuclear Instruments and Methods in Physics Research A*, 545:278–295, 2005.

[33] K. F. "Jack" Chen. CsI Calibration Using $K_L^0 \to 3\pi^0$ Decays. Internal Tech-Note, 2005.

[34] T. Inagaki et al. Detection inefficiency of a 10 mm thick plastic scintillation counter for 1 GeV/c $e^{\pm}$, $\pi^{\pm}$ and protons. *Nuclear Instruments and Methods in Physics Research A*, 359:478–484, 1995.

[35] CERN Program Library Long Writeup W5013. GEANT - Detector Description and Simulation Tool, 1993.

[36] Y. Tajima et al. Barrel photon detector of the KEK $K_L^0 \to \pi^0\nu\bar{\nu}$ experiment. *Nuclear Instruments and Methods in Physics Research A*, 592:261–272, 2008.

[37] T. Sumida. *Search for the decay* $K_L \to \pi^0\nu\bar{\nu}$. PhD thesis, Kyoto University, 2008.

[38] G. Battistoni et al. The FLUKA code: Description and benchmarking. *Proceedings of the Hadronic Shower Simulation Workshop 2006, Fermilab 6–8 September 2006, M. Albrow, R. Raja eds., AIP Conference Proceeding 896, 31-49, (2007).*

[39] A. Fasso‘ et al. FLUKA: a multi-particle transport code. *CERN-2005-10 (2005), INFN/TC_05/11, SLAC-R-773.*

[40] H. Watanabe. A Fusion Finder Using Neural-Net. 2004.

[41] R. Cousins and V. Highland. Incorporating systematic uncertainties into an upper limit. *Nuclear Instruments and Methods in Physics Research A*, 320:331–335, 1992.